The Eocene-Oligocene Transition

as a cascading tipping event

Bachelor's Thesis by Martijn E. Clemenkowff
Student number: 5978157
Programme: Physics and Astronomy
Institute for Marine and Atmospheric research Utrecht (IMAU)
Department of Physics, Utrecht University
Supervision by dr. A.S. von der Heydt

Abstract

The global climate transition which occurred approximately 33.7 Ma ago at the Eocene-Oligocene transition is characterised by a still largely unexplained two step cooling of the Earth, separated by a 200 kyr plateau visible in proxy data. Study by Tigchelaar et al. (2011) [36] suggests the potential explanation where a transition in the ocean overturning circulation induces the inception of Antarctic land ice, effectively cooling the Earth in a step-wise manner. In this thesis, we will discuss the behaviour of cascading fold bifurcating dynamical systems, as introduced by Dekker et al. (2018) [7], and apply these concepts to the ocean and land ice systems, to argue that the Earth's climate can be interpreted as such a cascading system. Through numerical simulation using the box model devised by Gildor and Tziperman (2000, 2001) [12,13], Gildor et al. (2002) [14], and subsequently adapted by Tigchelaar et al. (2011) [36], we present qualitative manifestations of this cascading behaviour, and argue that stochastic noise or insolation variability has the potential to induce the plateau observed in proxy data.

Contents

Introduction

One of the most distinct global climate transitions from a 'Greenhouse' to a partly glaciated Earth occurred near the Eocene-Oligocene (E-O) boundary, 33.7 Ma ago. The Eocene climate was considerably warmer than it is at the present day, with polar surface and deep water temperatures up to 10°C higher than today. The Antarctic continent already lay at its current latitude, but was ice-free and lushly vegetated in contrast to its present appearance. The transition away from this state of climate, is in biology often referred to as the Grande Coupure, or the 'great break' in continuity of mammalian fauna, due to the large-scale extinction that occurred at this time. From many climate proxies it is deduced that at the E-O boundary, global temperatures dropped and a semi-permanent ice sheet was formed on the Antarctic continent (Lear et al., 2000; Dockery and Lozouet, 2003; Coxall and Pearson, 2007; Liu et al., 2009) [2,10,20,21].

Some of the most pronounced evidence in support of such a cooling event comes from the marine benthic δ^{18}O record, which in numerous cores taken from the ocean floor, shows an increase of $1.2 - 1.5‰$ during this period. The shift lasts for approximately 500 kyr and most remarkable is the fact that this transition takes places in two steps, both lasting approximately 40 kyr, separated by a 200 kyr plateau during which the δ^{18}O remained approximately stagnant. The E-O transition ends with a sustained maximum lasting 400 kyr, after which δ^{18}O decreases again in a step-wise manner (Coxall et al., 2005) [3], to eventually stabilise at a value $\sim 1‰$ higher than before the transition (Zachos et al., 1996; Zachos and Kump, 2005; Coxall and Pearson, 2007) [3,43,44]. The rapid increase in δ^{18}O is associated with a rapid and extensive glaciation of at least the Antarctic continent, an hypothesis supported by glaciomarine sediments in the vicinity of the continent. Although there is geological evidence for Northern Hemispheric land ice dating back to the middle Eocene, data is insufficient to determine the extent of a Northern Hemisphere glaciation at this time (Eldrett et al., 2007) [11].

It is believed that, during the Eocene, deep water formation was more pronounced in the Southern than in the Northern Ocean. Sedimentary and seismic evidence, in combination with the analysis of neodymium isotopes, suggests that at the beginning of the Oligocene, a transition from such a southern sinking circulation (SPP) to a bipolar deep water formation (TH) occurred (Thomas et al., 2003; Thomas, 2004; Via and Thomas, 2006) [37,38,40]. The initiation of deep water formation in the North Atlantic Ocean was facilitated by the subsidence of the Greenland-Scotland Ridge which may have occurred around the E-O boundary (Davies et al., 2001) [5].

One mechanism which has been studied as a potential explanation for the Eocene-Oligocene transition is the opening of the Drake Pasage between Antarctica and South-America and of the Tasmanian Passage between Antarctica and Australia, facilitating the organization of an Antarctic Circumpolar Current (ACC). This would reduce southward oceanic heat transport, effectively cooling the Southern ocean and, having occurred around the Eocene-Oligocene boundary, it might have played a role in glaciation of the Antarctic continent. However, determining the exact timing of the opening of these passages has proven problematic (Livermore et al., 2005; Scher and Martin, 2006; Coxall and Pearson, 2007) [2,22,29] and the influence of a colder Southern ocean on Antarctic meteorology is poorly resolved (DeConto and Pollard, 2003) [6]. Other model and data studies support the notion of the development of an ACC promoting Antarctic ice inception, but not as the ultimate cause (Sijp and England, 2004; Sijp et al., 2009; Cramer et al., 2009; Haywood et al., 2010) [4,16,33,34].

Tigchelaar et al. (2011) [36] proposes the transition between two stable states of the meridional overturning circulation (MOC) as a mechanism for the E-O transition. In this model study the first increase in marine benthic δ^{18}O values is the result of the MOC transition from an SPP to a TH overturning state, i.e. a southern-only deep water formation to a bipolar deep water formation. This transition leads to a cooling of the deep ocean and thus an initial increase in marine benthic δ^{18}O. The second step is induced by lowering the atmospheric pCO2 below a critical threshold value, for which Antarctic land ice will rapidly grow, further increasing the marine benthic δ^{18}O values. It was found that the shift in MOC can occur spontaneously by random density fluctuations or induced by tectonic changes, i.e. the subsidence of the Greenland-Scotland Ridge and/or the opening of the Drake Passage and Tasman Gateway. The results of this model study where qualitatively in accordance with proxy data, but both these steps were still studied independent of each other. In Dekker et al. (2018) [7] a first attempt was made to study this system in the context of bifurcation theory; in terms of a cascade of rapidly transitioning systems, i.e. a cascading tipping event.

In this thesis, we will further expand on previous research by Tigchelaar et al. (2011) [36] and Dekker et al. (2018) [7], and investigate to what extent the E-O transition can be described as a cascading tipping event. We will discuss the mathematical framework of bifurcating systems, cascading tipping events and the effects of stochastic noise. The multiple stable climate equilibria as found by Tigchelaar et al (2011) [36] will be reintroduced, after which we will argue from simple coupled quasi-analytical ocean and land ice models that the cli-

mate system can be interpreted as a cascaded tipping system. Using a model developed by Gildor and Tziperman (2000, 2001) [12,13], Gildor et al. (2002) [14], and subsequently adapted by Tigchelaar et al. (2011) [36] for study of the Eocene climate, we will present and qualitatively analyse different (cascading) transition scenarios. This model, comprising 4 atmosphere boxes, 8 ocean boxes, with added land and sea ice components and a biogeochemistry module, will be comprehensively described in Section 4. Furthermore, we will investigate the possible effects of orbital variations on the time scales within the cascading transition.

Part I

Theoretical Framework

1 Bifurcating systems

1.1 Saddle-node bifurcations

In mathematical bifurcation theory, a saddle-node bifurcation or a fold bifurcation is characterised as a local bifurcation in which two equilibria of a dynamical system collide and annihilate each other. A typical example of a differential equation which has one saddle-node bifurcation is

$$\frac{dX}{dt} = a_1 + X^2, \tag{1.1}$$

where a_1 is a constant, X is a one-dimensional state variable and t is time. With steady states given by the condition $dX/dt = 0$, there are three different cases to discern:

1. $a_1 > 0$: no real solutions, thus no equilibria.
2. $a_1 = 0$: exactly one equilibrium at $X = 0$.
3. $a_1 < 0$: two equilibria at $\sqrt{-a_1}$ and $-\sqrt{-a_1}$, of which the first is unstable and the latter is stable[1].

The most generic form of a system which has a back-to-back saddle node bifurcation, and the one that is of interest for this subject matter, is given by the following differential equation;

$$\frac{dX}{dt} = a_1X^3 + a_2X + a_3, \tag{1.2}$$

where a_i with $i \in \{1, 2, 3\}$ are constants. It is proven in Appendix A. that this system has multiple equilibria if and only if $a_1 < 0, a_2 > 0$ and $|a_3| < \left(-4a_2^3/\left(27a_1\right)\right)^{1/2}$. Given that a_1 and a_2 satisfy these conditions, this system as a function of a_3 thus has a regime between $a_3 = \pm\left(-4a_2^3/\left(27a_1\right)\right)^{1/2}$ where there are multiple stable equilibria and outside this regime only one stable equilibrium prevails at each side (Fig. 1.1). We shall refer to the points where one of the two stable equilibria ceases to exist, as critical thresholds. This is thus one of the simplest systems which can undergo a rapid transition from one equilibrium to another as a function of a time-dependent parameter[2].

1.2 Double fold cascade

The simplest case which can exhibit a cascaded tipping event, is a system of two linearly coupled fold-bifurcating systems, i.e.

$$\begin{cases} \dfrac{dX}{dt} = a_1X^3 + a_2X + \phi(t), \\ \dfrac{dY}{dt} = b_1Y^3 + b_2Y + \kappa(X). \end{cases} \tag{1.3}$$

[1] see Appendix A.

[2] note that strictly speaking this parameter should vary infinitely slowly, something unattainable in numerical simulation of course.

Here a_i and b_i are constants, X is the leading system, Y is the following system, and $\kappa(X)$ is a linear coupling function given as $\kappa(X) = \kappa_1 + \kappa_2X$. $\phi(t)$ is a time-dependent variable which can be used to force the leading system into a transition.

In Fig. 1.1 we present the bifurcation diagram of the leading and following system for the values $\{a_1, a_2, b_1, b_2, \kappa_1, \kappa_2\} = \{-1, 1, -1, 1, -1.5, 1\}$ alongside a temporal evolution of this system where ϕ is linearly increased from $\phi = -10$ to $\phi = 10$ throughout the simulation in Fig. 1.2. Directly apparent is the distinct two step mechanism present in the temporal evolution of the following system; this is also support by the bifurcation diagram of the following system where we see two subsequent regions where there are two different stable equilibria in the system. When considering this system for $\{a_1, a_2, b_1, b_2, \kappa_1, \kappa_2\} = \{-1, 1, -1, 1, 0, 1\}$, one can also find the situation where in the region of bifurcation all equilibria overlap. In the time evolution this is simply reflected as a single step mechanism in the following system instead of two steps. Another interesting limit case was found by Dekker et al. (2018) [7] for $\{a_1, a_2, b_1, b_2, \kappa_1, \kappa_2\} = \{-0.5, 0.5, -0.5, 1, 0, 0.48\}$ where there are four stable equilibria overlapping with each other.

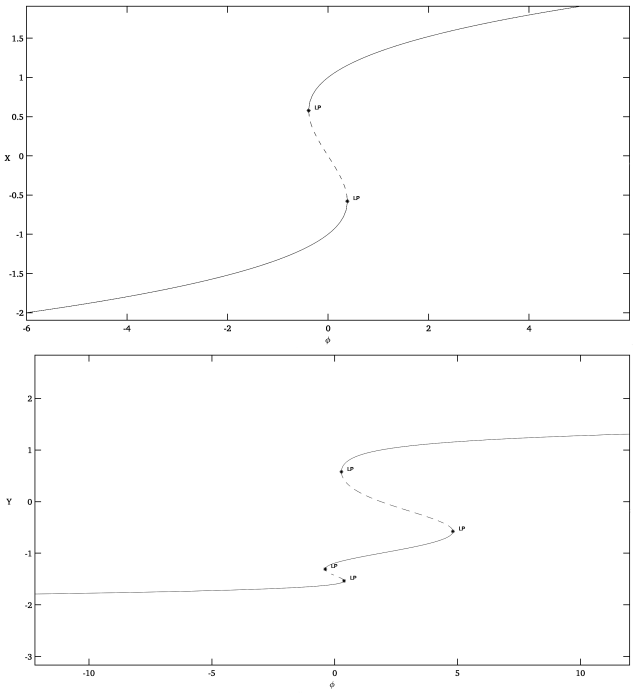

Fig. 1.1: Bifurcation diagram for the leading system X (top) and the following system Y (bottom) as in Eq. 1.3 for $\{a_1, a_2, b_1, b_2, \kappa_1, \kappa_2\} = \{-1, 1, -1, 1, -1.5, 1\}$.

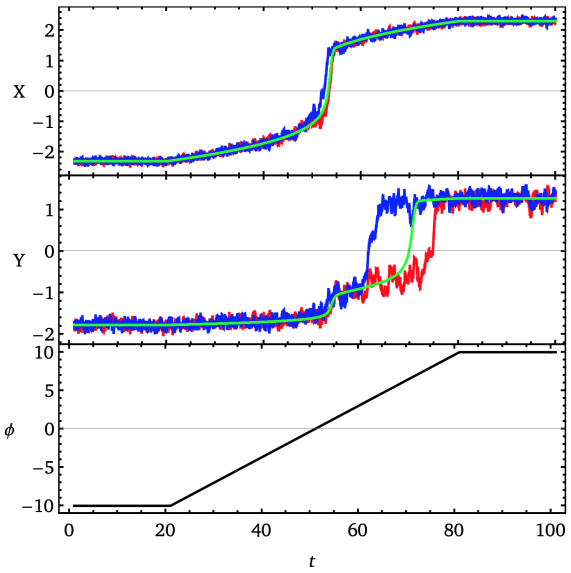

Fig. 1.2: Temporal evolution of the leading and following system X and Y as in Eq. 1.3 and Eq. 1.4 for $\{a_1, a_2, b_1, b_2, \kappa_1, \kappa_2\} = \{-1, 1, -1, 1, -1.5, 1\}$, alongside the forcing $\phi(t)$. Simulation without noise is shown in green. Two simulations with different seeds of Gaussian white noise are shown in blue (**numpy.random.seed(11)**) and red (**numpy.random.seed(10)**).

1.3 Stochastic advance and delay

An extensive analysis of the effects of a noise term on cascading systems like this has been conducted by Dekker et al. (2018) [7]. The effects discussed there encompass phenomena like stochastic flickering, where the following system randomly transitions between two equilibria, but in this study we are most interested in the effects stochastic noise can have on the timing of the transitions. We introduce a Gaussian white noise term ζ_x and ζ_y to the leading and following system respectively, hence our system becomes

$$\begin{cases} \dfrac{dX}{dt} = a_1 X^3 + a_2 X + \phi(t) + \zeta_x, \\ \dfrac{dY}{dt} = b_1 Y^3 + b_2 Y + \kappa(X) + \zeta_y. \end{cases} \tag{1.4}$$

We set $\zeta_x = \zeta_y = \zeta$, $\bar{\zeta} = 0$ and $\sigma(\zeta) = 10$ and consider the system for two different seeds of white noise[3]. The time evolution of this system is presented in Fig. 1.2, alongside the system without noise. We can clearly observe that the added white noise can either advance or delay the transitions within the system. This is readily explained by the fact that depending on the phase of the noise, the system crosses the critical thresholds earlier or later than it would have as a result of only the linear increase of ϕ. As the newly attained stable equilibrium also exists for forcing below the critical threshold[4], when the noise term becomes negative the system does not directly transition back to the original equilibrium. For both this case and the case of stochastic flickering, the white noise introduces a component of internal variability to both the leading and following system which allows for tipping independent of external forcing or forcing through the leading system in the case of tipping in the following system.

[3] this simulation was executed in Python; we consider **numpy.random.seed(10)** and **numpy.random.seed(11)** here.

[4] you could interpret this as a two-way hysteresis.

2 The climate system

2.1 The Meridional Overturning Circulation (MOC)

In the Earth climate system, a wide range of components interact with each other on a variety of temporal and spatial scales. Among these systems are the atmosphere, the oceans, land and sea ice, the terrestrial biosphere and ocean biochemistry, under the external forcing of, among others, solar insolation and variations in this as a result of orbital variability, plate tectonics and volcanism. One of the most important components of the climate system on both local and global scale is the ocean circulation, and specifically the system of the large scale meridional flows which we refer to as the meridional overturning circulation (MOC). At present day, this circulation is characterised by flow of warm, salty water from the equator towards both poles, where the water cools and sinks, giving rise to transport of colder water back towards the equator in the deep ocean. This circulation is a major driver of meridional heat transport, as it interacts with the overlaying atmosphere, and its varying strength has cautiously been related to global climate change and the glacial-interglacial cycles (Mcmanus et al., 2004; Ivanovic et al., 2017) [18,25]. As we will see in Sec. 2.2 there exist more stable states of this overturning circulation than just the one we observe at the present day, and as noted in the introduction, there is geological evidence suggesting that a transition between such two different equilibria occurred at the Eocene-Oligocene boundary.

2.2 Multiple overturning equilibria

Differential heating of the Earth's surface leads to warm, salty equatorial surface waters, and relatively cooler, fresh polar surface waters. The effect of this, is that temperature and salinity play opposing roles in determining surface flow direction and hence the location of deep water formation. This suggests that multiple MOC patterns exist. This notion was studied by Stommel (1961) [35] using a density driven two-box model[1] representing a single hemisphere, with which he showed two different states of the MOC to exist on a single hemisphere; sinking in the polar box or sinking in the equatorial box. An extended version of this model with three boxes (two polar boxes and one equatorial box) (Welander, 1986; Thual and McWilliams, 1992) [41] allows for four solutions: sinking in the North and upwelling in the South (NPP), sinking in the South and upwelling in the North (SPP), bipolar sinking (TH) and bipolar upwelling (SA). These different overturning patterns are also observed in more sophisticated 3D models (Dijkstra and Weijer, 2003) [8], however the SA pattern has never really been observed in such models. Following the emphasis put by Tigchelaar et al. (2011) [36] on an SPP-TH overturning transition for the Eocene-Oligocene boundary, throughout this study only the SPP and TH overturning states are of interest.

In Fig. 2.1 we present the flow patterns and average atmosphere and ocean temperatures for a southern sinking (SPP) overturning and for a bipolar sinking (TH) overturning equilibrium state. These diagrams are the result of numerical simulation using the Gildor-Tziperman model (Gildor and Tziperman, 2000, 2001; Gildor et al., 2002) [12–14] which we will describe and utilise later in Part 2. Directly apparent is the temperature difference between states for the Northern polar atmospheric and surface ocean boxes; in the SPP state there is slight upwelling in the Northern polar ocean, i.e. cold deep ocean water rising to the surface, effectively cooling the surface ocean and atmosphere. In the TH state on the other hand, there is significant downwelling in the Northern polar ocean, which occurs in conjunction with the transport of warm water from the equatorial latitudes to the polar latitudes along the surface, effectively warming the Northern polar surface ocean and atmosphere. Due to the differential distribution of the total energy budget between both states, all boxes other than the Northern polar surface ocean and atmosphere are cooler in the TH state than they are in the SPP state.

2.3 Milanković forcing

As was already first observed centuries ago, the Earths orbit around the Sun is not invariable, but is characterised by oscillations in precession, obliquity or axial tilt, eccentricity and the longitude of the perihelion. The link between these orbital variations and cyclical variations in the climate due to the resulting varying solar insolation was not first, but most notably, made by Milutin Milanković in the 1920's. As reliable geological evidence was limited at that time, it was not until 1976 (Hays et al., 1976) [15] that this hypothesis was truly accepted, but since then we bring these cyclical variations in the climate together under the name of the Milanković cycles. In Fig. 2.2 we present the typical timescales associated with the different components of the orbital variation. Obviously, these variations were also present during the Eocene/Oligocene, and a numerical solution devised by Laskar et al. (2004) [19] allows for accurate reconstruction of these variations up until 40-50 Myr ago, after which chaotic evolution of the Earth's orbit prevents further precise determination. While the Milanković forcing is generally of greatest interest for the glacial-interglacial cycles of the last 5 Myr, on the time scales we consider in this study it effectively can act as a pseudo-random noise with a very distinct frequency composition.

[1] now often referred to as the Stommel box model.

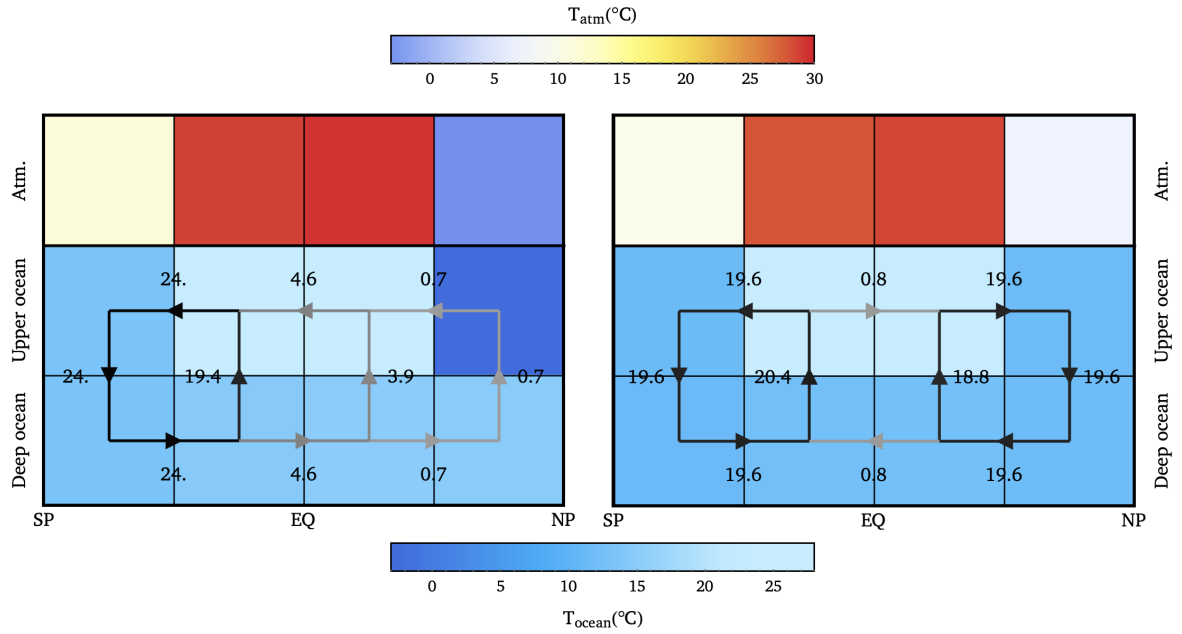

Fig. 2.1: Flow diagrams for southern sinking (SPP) overturning (left) and for bipolar sinking (TH) overturning. Flow magnitudes are denoted in Sv (10^6 m^3 s^{-1}). Box colours represent time averaged box temperatures.

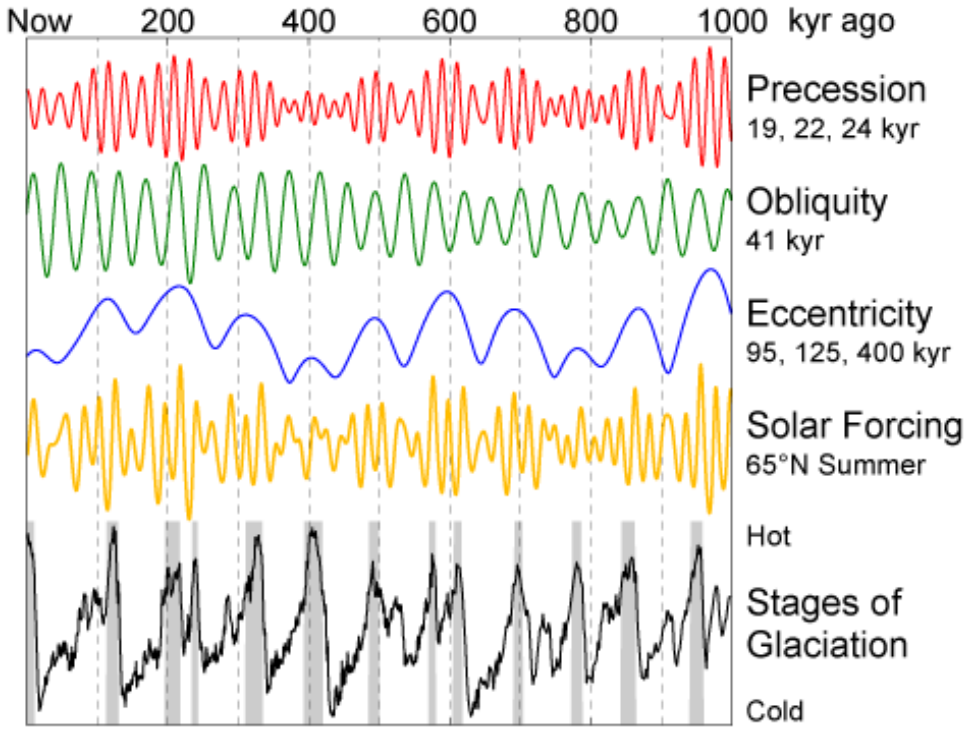

Fig. 2.2: Characteristic timescales of orbital variations. Figure originally by Rohde (2006) [28].

3 Interpretation as a cascading system

In this chapter we argue from simple isolated ocean and land ice models that the interaction between these two components of the climate system can display bifurcating behaviour analogous to the behaviour of double fold cascading systems. We will do so using the two-box ocean model devised by Stommel (1961) [35], the extended three-box variant of this model (Welander, 1986) [41] and the land ice model as in Oerlemans (2003) [27]. We shall discuss the formulation and bifurcation behaviour referencing the research of Dijkstra and Weijer (2003) [8] and Oerlemans (2003) [27].

3.1 Two-box ocean model

One of the simplest models for the description of the ocean circulation on one hemisphere, is the two-box model originally devised by Stommel. In this type of model the ocean on one hemisphere is divided into a polar box and an equatorial box, with T_p (S_p) and T_e (S_e) as respective box averaged temperatures (salinity). The two boxes are connected by an overflow region at the top and a capillary tube connecting the bottom of both boxes. This construction allows flow along the surface, which we consider positive when directed towards the polar box. A schematic representation of this model is presented in Fig. 3.3 at the end of this chapter. Even though this type of model is limited to representing only one hemisphere, we can use it in our analysis and it is a valuable mean to introduce the formulation that is also followed by the Welander three-box model.

3.1.1 Formulation

The flow in this model is density driven. The average density in each box is derived from both T and S around a reference density ρ_0, i.e.

$$\rho_i = \rho_0(1 - \alpha_T(T_i - T_0) + \alpha_S(S_i - S_0)), \tag{3.1}$$

where T_0 (S_0) is a reference temperature (salinity) and α_T (α_S) the thermal (saline) expansion coefficient. The evolution of T and S in each box is assumed to be dictated only by exchange through flow[1], heat exchange with the overlaying atmosphere and a constant freshwater forcing between boxes for the salinity (F). Under these assumptions the system of equations becomes

$$\begin{cases} V_p \dfrac{dT_p}{dt} = |q|\Delta T + c_p(T_{a,p} - T_p) \\ V_e \dfrac{dT_e}{dt} = -|q|\Delta T + c_e(T_{a,e} - T_e) \\ V_p \dfrac{dS_p}{dt} = |q|\Delta S - F \\ V_e \dfrac{dS_e}{dt} = -|q|\Delta S + F, \end{cases} \tag{3.2}$$

where $\Delta T = T_e - T_p$, $\Delta S = S_e - S_p$ and V_i are the box volumes, where $i = \{p, e\}$. The box temperature adjusts to a constant atmospheric temperature $T_{a,i}$ with c_i as the corresponding coefficients. Note however that this formulation inhibits us from dynamically modelling the atmosphere temperature, as the atmosphere is considered to be an infinite heat reservoir.

The flow strength is found from the density difference between both boxes as

$$q = -\frac{k}{\rho_0}(\rho_p - \rho_e) = k(\alpha_T \Delta T - \alpha_S \Delta S). \tag{3.3}$$

3.1.2 Bifurcating behaviour

From the bifurcation diagram presented in Fig. 3.1 we clearly see the two-box ocean model exhibits a distinct back-to-back saddle node bifurcation in the flow strength as a function of the freshwater flux. The figure presented here is originally from Dijkstra and Weijer (2003) [8] and this publication uses ψ for the dimensionless flow strength and λ denotes the dimensionless freshwater flux. For weak freshwater fluxes there exists only a TH/NPP[2] state, where there is sinking in the Northern oceanic box. For strong freshwater fluxes we find an SA/SPP state[3], i.e. upwelling in the Northern oceanic box. Between these regions of single stable equilibria there is a region where both overturning states are equally stable, which thus allows for tipping behaviour.

3.2 Three-box model

The Welander three-box model is the simplest iteration of the ocean box model with which the interaction between both hemispheres can be represented. This model comprises two polar boxes, and one equatorial box representing the tropical regions of both hemispheres. The coupling of both polar boxes with the equatorial box are identical to the Stommel box model formulation. A schematic representation of this model is presented in Fig. 3.4 at the end of this chapter.

[1] where the direction of the flow is not important.

[2] while we only consider one hemisphere here, TH and NPP overturning states are indistinguishable.

[3] as previous footnote, but for SA and SPP overturning states.

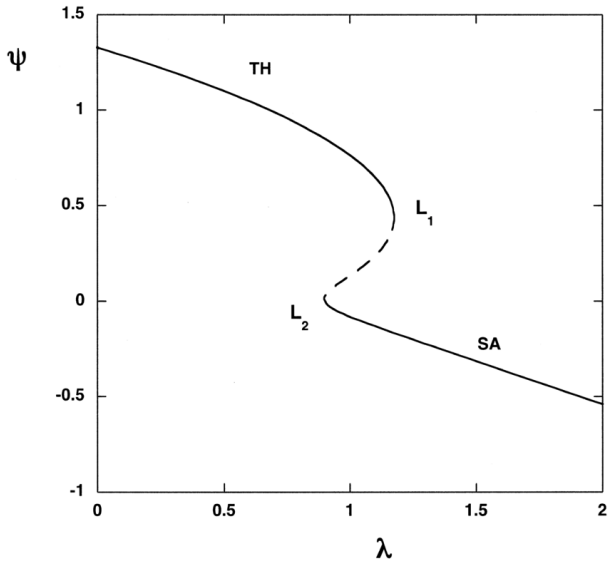

Fig. 3.1: Bifurcation diagram of the two-box ocean model as originally published by Dijkstra and Weijer (2003) [8]. Dimensionless flow strength ψ as a function of dimensionless freshwater flux λ.

3.2.1 Formulation

The Welander three-box model follows the same formulation as the Stommel box, merely extended to three boxes. The system of equations becomes

$$\begin{cases} V_s \dfrac{dT_s}{dt} = |q_s|\Delta T_s + c_s(T_{a,s} - T_s) \\ V_e \dfrac{dT_e}{dt} = -|q_s|\Delta T_s - |q_n|\Delta T_n + c_e(T_{a,e} - T_e) \\ V_n \dfrac{dT_n}{dt} = |q_n|\Delta T_n + c_n(T_{a,n} - T_n) \\ V_s \dfrac{dS_s}{dt} = |q_s|\Delta S_s - F_s \\ V_e \dfrac{dS_e}{dt} = -|q_s|\Delta S_s - |q_n|\Delta S_n + F_s + F_n \\ V_n \dfrac{dS_n}{dt} = |q_n|\Delta S_n - F_n, \end{cases} \tag{3.4}$$

$$q_i = k(\alpha_T \Delta T_i - \alpha_S \Delta S_i). \tag{3.5}$$

where $\Delta T_i = T_e - T_i$, $\Delta S_i = S_e - S_i$ and q_i with $i \in \{s, n\}$ are the temperature difference, salinity difference and flow between respectively the Southern and equatorial, and Northern and equatorial boxes.

3.2.2 Bifurcating behaviour

The bifurcation diagrams (Dijkstra and Weijer, 2003) [8] presented in Fig. 3.5 show a considerable increased level of complexity for the three-box model relative to the two-box model. Here we recognise all four overturning states (TH, SA, NPP and SPP), where in the case of a symmetric freshwater forcing it is apparent that the NPP and SPP states exist besides each other. For weaker freshwater fluxes both states fall back to the TH overturning, while for stronger freshwater fluxes the symmetric overturning is of the SA type. In this situation there is only a fast transition possible from an SPP to an NPP state, but more options are present when the freshwater forcing is asymmetric. The bifurcation diagram splits into two detached branches, consequently allowing for fast transitions between all combinations of asymmetric (NPP, SPP) and symmetric (TH, SA) overturning circulations.

3.3 Land ice model

3.3.1 Formulation

In the construction of this model we follow the formulation by Oerlemans (2003) [27]. We assume the Antarctic ice sheet to be perfectly plastic and approximately axisymmetric around the South Pole. This yields that the height h of the ice is simply proportional to the square root of the radial distance r from the South Pole, i.e.

$$h(r) = \big(\mu_0(R - r)\big)^{1/2}. \tag{3.6}$$

Here R is the radius of the ice sheet, r is the radial position and μ_0 is the profile parameter. Furthermore, we assume that the undisturbed bed rock on which the ice sheet lays slopes linearly downwards away from the centre of the ice sheet. The bed rock height $d(r)$ is given as

$$d(r) = d_0 - sr, \tag{3.7}$$

where d_0 denotes the undisturbed height of the bed at the centre and s is the slope. We assume that s has no effect on the surface profile or characteristics. Note however that for a given value of d_0, the mean surface elevation decreases for increasing s. This is taken into account by formulating the ice sheet profile as follows;

$$h(r) = d_0 - sR + \big(\mu(R - r)\big)^{1/2}, \tag{3.8}$$

where

$$\mu = \mu_0 + cs^2, \tag{3.9}$$

with c a constant which is chosen based on numerical experimentation.

In this present study we will not include calving of ice into the ocean. Under this simplification, and initially ignoring the response of the bed to the ice load, we can find the total volume of the ice sheet through straightforward polar integration, i.e.,

$$V = 2\pi \int_0^R h(r)\, r\, dr = \frac{8\pi\mu^{1/2}}{15} R^{5/2} - \frac{1}{3}\pi s R^3. \tag{3.10}$$

However, the interesting non-linear behaviour of the ice sheet originates from the dependence of the mass budget B_{tot} on the shape of the ice sheet. To formulate an expression for the mass budget as a function of the ice height, we introduce the concept of the run-off line,

denoted by h_R. Above the run-off line the mass balance B is constant, while below the run-off line the balance gradient with respect to altitude is constant. As such, we define

$$\begin{cases} B = A & \text{for } h \geq h_R \\ B = A - \beta(h_R - h) & \text{for } h < h_R, \end{cases} \tag{3.11}$$

where A is the accumulation and β is the balance gradient with respect to altitude. The more commonly used altitude of the equilibrium line h_E relates to h_R as

$$h_E = h_R - A/\beta \tag{3.12}$$

For a continental ice sheet we find the total mass budget B_{tot} to be

$$\begin{aligned} B_{tot} &= \int_0^{2\pi} \int_0^{R} B\, r\, dr\, d\phi \\ &= \pi A R^2 - \pi\beta(h_R - d_0 + sR)\left(R^2 - r_R^2\right) \\ &+ 4\pi\beta\mu^{1/2}\left(\frac{1}{5}(R - r_R)^{5/2} - \frac{1}{3}R(R - r_R)^{3/2}\right), \end{aligned} \tag{3.13}$$

where

$$r_R = R - \mu^{-1}(h_R - d_0 + sR)^2 \tag{3.14}$$

is the radial position at which the runoff line intersects the ice sheet surface. Now equilibrium states of R can be found by setting $B_{tot} = 0$ and using either numerical root-finding algorithms, or integrating the time evolution of the ice volume $dV_{tot}/dt = B_{tot}$, which we did not discuss here but is extensively explained in Oerlemans (2003) [27].

3.3.2 Bifurcating behaviour

Study of the bifurcating behaviour of this ice sheet model by Oerlemans (2003) [27] found a structure reminiscent of a back-to-back fold bifurcation. Considering the ice extent R as a function of the difference between the equilibrium height and the highest point of the surface elevation, $R = 0$ is a stable solution for the whole parameter space. However, due to the constraint $R \geq 0$, this solution is only valid for $h_E - d_0 \geq 0$. Additionally a second branch is found where $R > 0$, and this branch overlaps with the $R = 0$ branch in the parameter space. An unstable branch (not shown here) connects both limit points. This reflects the hysteresis effect which is a known phenomenon in ice dynamics; due to the ice-albedo and height-mass feedbacks an existing ice sheet can stably persist for climate scenarios which would not allow for new ice inception.

3.4 Proposed coupling

Assuming that the atmospheric temperature adjusts to the ocean temperature, the ocean and land ice models could potentially be coupled linearly via the Southern ocean temperature T_s and the equilibrium height h_E, i.e.

$$h_E = h_{E,0}(1 - k_E(T_{s,0} - T_s)), \tag{3.15}$$

where $h_{E,0}$ and $T_{s,0}$ are respectively a reference equilibrium height and Southern ocean temperature and k_E is a coupling coefficient. As such this ocean - land ice system would take the form of the generic cascading fold-fold system we discussed in Sec. 1.2 where the ocean is the leading system, and the ice sheet is the following system.

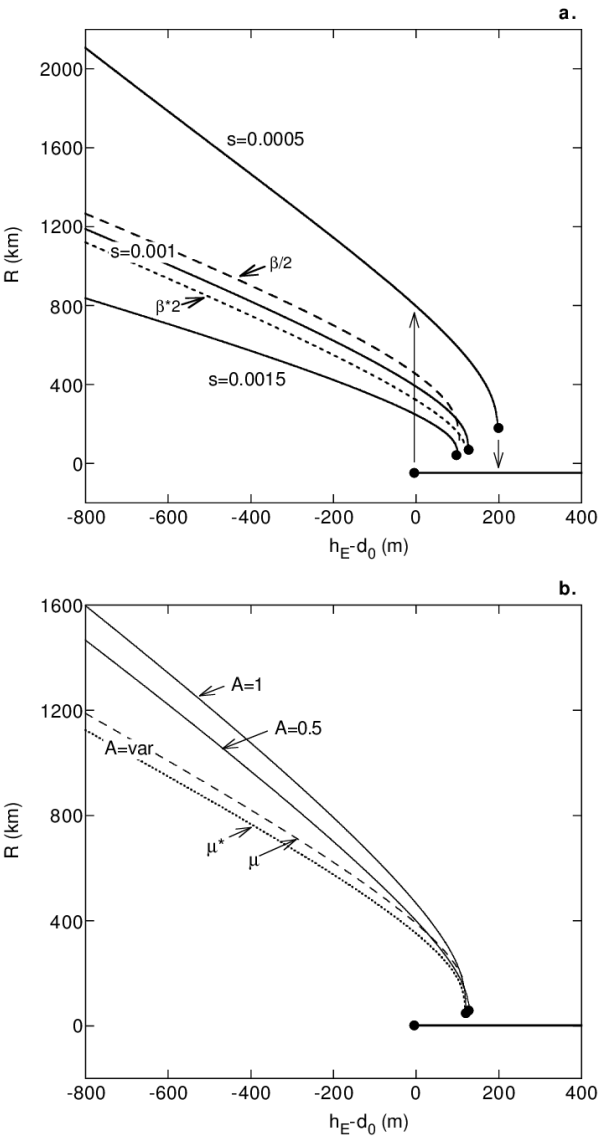

Fig. 3.2: Bifurcation diagram of the land ice sheet model as originally published by Oerlemans (2003) [27].

3.5 Preliminary conclusions and shortcomings

The isolated bifurcation behaviour of both the ocean and land ice models reflect characteristics of the elementary fold bifurcating systems discussed in Sec. 1.1. Through a simple linear relation one would expect the coupled system, where the ocean is the leading system and the land

ice sheet is the following system, to reflect the temporal evolution observed in Sec. 1.2. The linear coupling approach proposed here has little physical validity however besides making the argument for the cascading tipping hypothesis. A more physically correct coupling should relate the Southern atmospheric temperature to the equilibrium height, but in doing so an actively modelled atmosphere becomes a necessity, complicating the model further than what is within the scope of this present thesis. However, as we will see in Part 2, the changes in Southern ocean and atmospheric temperatures for a transition from an SPP overturning to a TH overturning are comparable in magnitude, thus still allowing for this argument to be made.

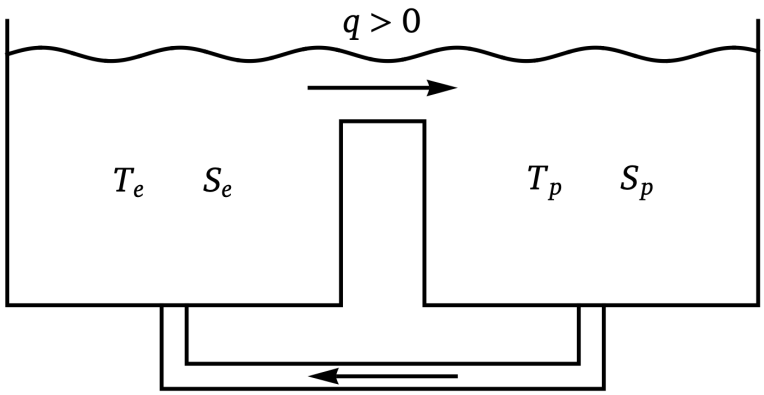

Fig. 3.3: Schematic representation of the Stommel box ocean model.

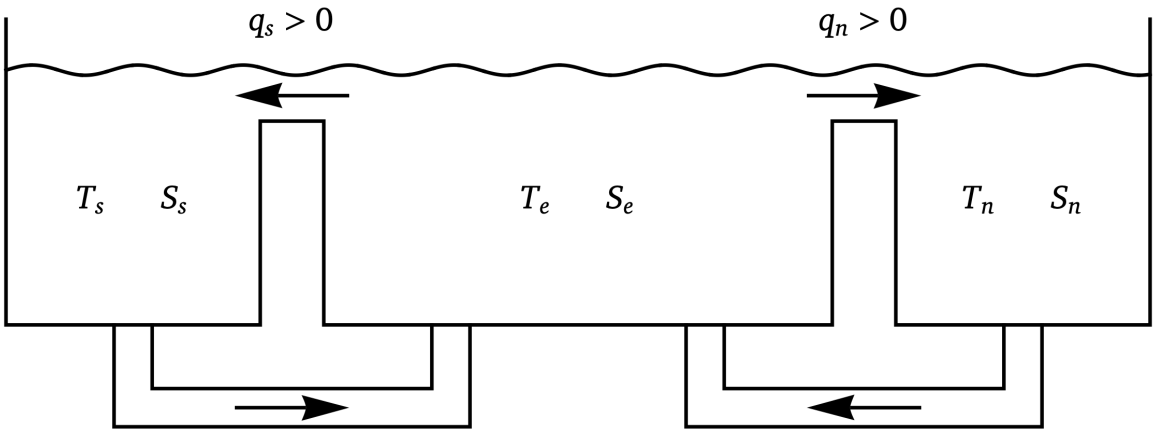

Fig. 3.4: Schematic representation of the Welander three-box ocean model.

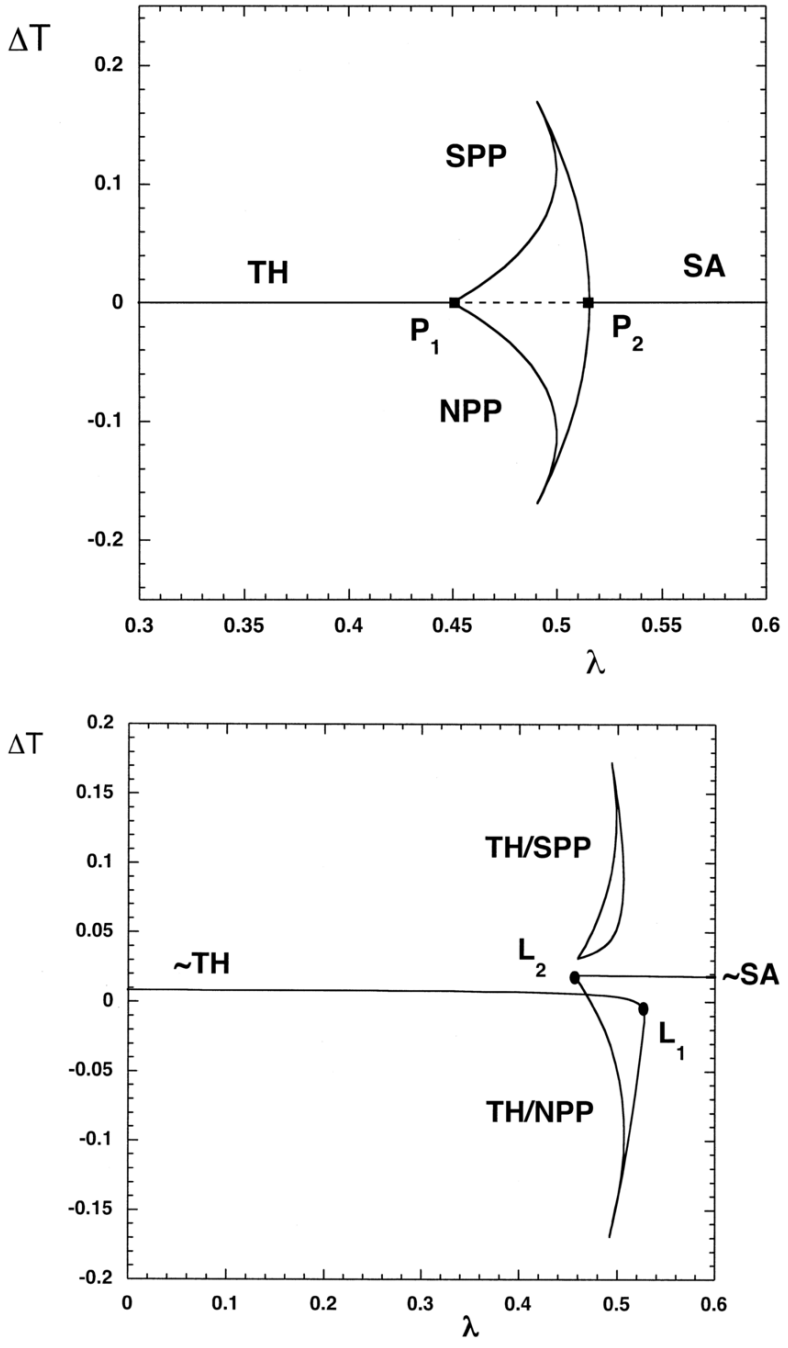

Fig. 3.5: Bifurcation diagram of the two-box ocean model as originally published by Dijkstra and Weijer (2003) [8], showing North-South polar temperature difference as a function of a symmetric (asymmetric) dimensionless freshwater flux λ in top (bottom) panel.

Part II

Earth System Approach to Cascading Tipping

4 Model description

General layout

The model described here is the 4+8 climate box model developed by Gildor and Tziperman (2000, 2001) [12,13] and Gildor et al. (2002) [14], originally intended for study of the glacial-interglacial cycles, and subsequently adapted by Tigchelaar et al. (2011) [36] for study of the Eocene climate. This model comprises four vertically averaged atmospheric boxes, which extend latitudinally from the South Pole to 45°S, from 45°S to equator, from equator to 45°N and lastly from 45°N to the North Pole. These boxes overlay eight ocean boxes divided into two layers; four representing the upper ocean and four for the deep ocean, all spanning the same latitude bands as the atmospheric boxes. In this study we will disregard the effect of sea ice as explained in Sec. 4.7.

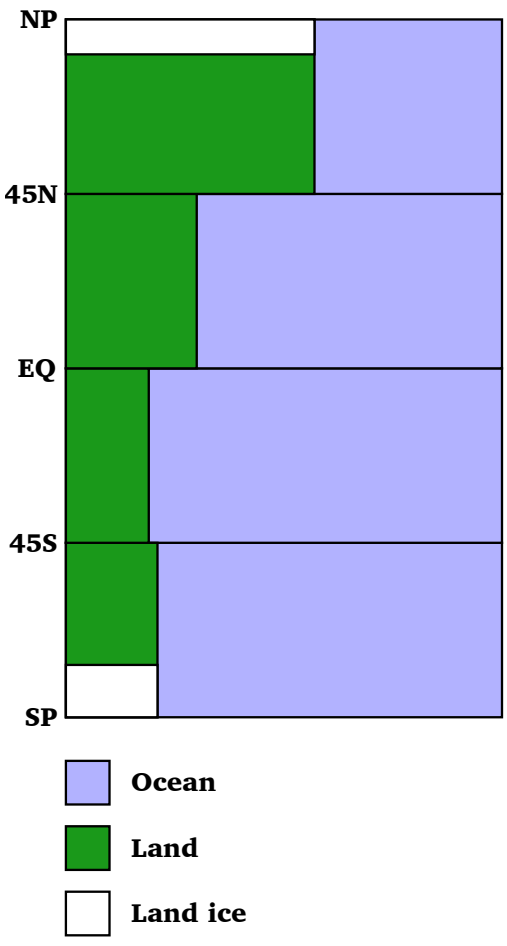

Fig. 4.1: Top view of the Gildor-Tziperman model, indicating ocean, land and land ice fractions.

4.1 Atmosphere model

As stated in the previous section, the atmosphere is described by four atmospheric boxes laying above the ocean boxes; a polar and an equatorial box for each hemisphere. The lower interface can be either land or ocean, where the land/ocean fractions for each box are dictated by estimates of the Eocene geography, as in Tigchelaar et al. (2011) [36] (Fig. 4.1). Land fractions in the polar boxes can be partially covered by land ice. The box averaged potential temperature is calculated from the energy balance in the box, comprising incoming solar radiation and outgoing longwave radiation, air-ocean heat flux and meridional atmospheric heat transport. The potential temperature of each box is determined by the difference between the heat flux at the top of the atmosphere (F_{top}) and at the surface ($F_{surface}$), i.e.

$$\begin{aligned}\frac{\partial\theta}{\partial t} &= \frac{2^{R/C_p}g}{p_0 C_p}\left[\left(F_{top}-F_{surface}\right)+\left(F^{in}_{merid}-F^{out}_{merid}\right)\right]\\ &= \frac{2^{R/C_p}g}{p_0 C_p}\left[\left(H_{in}-H_{out}-Q_{T,a}\right)+\left(F^{in}_{merid}-F^{out}_{merid}\right)\right],\end{aligned} \tag{4.1}$$

with respectively the incoming and outgoing radiation terms at the top of the atmosphere defined as

$$\begin{aligned}H_{in} &= (1-\alpha_{surf})(1-\alpha_C)Q_{Sol}\\ H_{out} &= \left(\epsilon-\kappa\ln\frac{[CO_2]}{[CO_2]_0}\right)\sigma_B\theta^4.\end{aligned} \tag{4.2}$$

Here R is the gas constant for dry air, C_p is the specific heat capacity of the atmosphere at constant pressure, p_o is a reference pressure, σ_B is the Stefan-Boltzmann constant and g is the gravitational acceleration. The incoming solar radiation Q_{sol} varies seasonally and as a result of orbital variations, with the latter modelled using the model devised by Berger (1978) [1]. α_C is the cloud albedo and α_{surf} is the surface albedo defined as

$$\alpha_{surf} = f_L(1-f_{LI})\alpha_L + f_L f_{LI}\alpha_{LI} + f_O\alpha_O, \tag{4.3}$$

with f_L, $f_L I$, f_O the land, land ice and ocean fractions respectively. Corresponding typical albedoes are denoted with the same subscripts. The outgoing radiation is determined by a mean box emissivity ϵ and a logarithmic term depending on the the ratio between the atmospheric CO_2 concentration and a reference concentration $[CO_2]_0$, where κ is chosen such that an instant doubling of the CO_2 concentration will cause a radiative forcing of 4 Wm^{-2} in accordance with contemporary climate sensitivity. $Q_{T,a}$ is the heat flux between the atmosphere and ocean which we will further quantify when discussing the ocean model (Sec. 4.3).

Lastly concerning the energy balance, $F^{in}_{merid} - F^{out}_{merid}$ is the effective heating due to meridional heat transport

between atmospheric boxes. Meridional heat fluxes are calculated as

$$F_{merid} = K_\theta \nabla\theta, \tag{4.4}$$

with K_θ chosen such that the meridional heat transport between the two Northern hemispheric boxes is $\sim$ 2.2 PW during interglacial periods (Gildor and Tziperman, 2001) [13].

Concluding the atmosphere model, the meridional moisture transport F_{Mq} between atmospheric boxes is parametrised as

$$F_{Mq} = K_{Mq}|\nabla\theta|q, \tag{4.5}$$

with q the humidity in the box of concern and K_{Mq} a constant. We assume a constant relative humidity, with the saturation humidity at the potential temperature θ computed from an approximate Clausius-Clayperon equation;

$$q = 0.7Ae^{B/\theta}, \tag{4.6}$$

with A and B constants. Over land ice in the polar boxes there is an additional source of precipitation, which is the local evaporation of the ocean not covered by sea ice;

$$F_q = K_q f_{ow} q, \tag{4.7}$$

where f_{ow} is the surface fraction of open water relative to a surface fraction of sea ice f_{si} with $f_{ow} = 1 - f_{si}$, and K_q is a constant. The total precipitation in each box is then given as

$$P - E = -\nabla \cdot (F_{Mq} - F_q), \tag{4.8}$$

where P and E are respectively the precipitation and evaporation in the box of concern. Precipitation falling over land/sea ice is assumed to turn into additional land/sea ice.

4.2 Land ice model

The main equation for the land ice model is a simple mass balance, i.e.

$$\frac{dV_{land\ ice}}{dt} = LI_{source} - LI_{sink}. \tag{4.9}$$

The source term LI_{source} depends on the precipitation falling over existing land ice or, if there is no existing land ice present at these positions, 1/4 of the land area of the box;

$$LI_{source} = \frac{\max\left(\{0.25L_{area},\, LI_{area}\}\right)}{box_{area}}(P - E), \tag{4.10}$$

where L_{area} is the land area in the box, LI_{area} the ice sheet area, box_{area} the total area of the box. The ice sheet shrinks due to a constant ablation term C_{LI}, plus an extra modulation by the summer Milanković forcing, i.e.

$$LI_{sink} = C_{LI} + \gamma_{LI}(S_{june} - \bar{S}_{june}) \tag{4.11}$$

where $S_{june} - \bar{S}_{june}$ is the anomaly in the summer insolation for the box of concern relative to the 1 Myr average. γ_{LI} is a constant used to tweak the sensitivity of the land ice to the summer Milanković forcing. The model will create ice when the local atmospheric temperature is below a threshold set as T_{melt}. These values may differ for both the Northern and Southern polar boxes and throughout this study we will vary T_{melt} for the Southern polar box, to control the inception of an Antarctic land ice sheet.

4.3 Ocean model

Due to the two-dimensional nature of the box model, the dynamics of the ocean model include a simple two-component frictional momentum balance which is hydrostatic and mass-conserving,

$$-\frac{1}{\rho_0}\frac{\partial p}{\partial z} - \frac{g}{\rho_0}\rho = 0, \tag{4.12}$$

$$-\frac{1}{\rho_0}\frac{\partial p}{\partial y} - rv = 0, \tag{4.13}$$

$$\frac{\partial v}{\partial y} + \frac{\partial w}{\partial z} = 0, \tag{4.14}$$

where (y, z) are the meridional and vertical coordinates and resp. (v, w) the corresponding flow velocities. g is the gravitational constant, p the pressure, ρ_0 a reference density and r a friction coefficient. The average density in each box is determined by the temperature T and the salinity S through the full nonlinear equation of state as recommended by UNESCO (1981) [39]. Temperature and salinity are determined by the following balances;

$$\begin{aligned}\frac{\partial T}{\partial t} + \frac{\partial (vT)}{\partial y} + \frac{\partial (wT)}{\partial z} = \\ K_h\frac{\partial T}{\partial y} + K_v\frac{\partial T}{\partial z} + Q_{T,a},\end{aligned} \tag{4.15}$$

$$\begin{aligned}\frac{\partial S}{\partial t} + \frac{\partial (vS)}{\partial y} + \frac{\partial (wS)}{\partial z} = \\ K_h\frac{\partial S}{\partial y} + K_v\frac{\partial S}{\partial z} + Q_{S,a} + Q_{S,LI}.\end{aligned} \tag{4.16}$$

Here K_h and K_v are resp. the horizontal and vertical mixing coefficients. $Q_{S,LI}$ is the salinity flux as a result of evaporation and ice formation. $Q_{T,a}$ is the atmosphere-ocean heat flux due to the sensible, latent and radiative fluxes, defined as

$$Q_{T,a} = \frac{\rho_0 C_{pw} D_u}{\tau}(\theta - T)\left[f_{ow} + f_{si}\frac{\gamma}{D_{si}}\right], \tag{4.17}$$

where C_{pw} is the heat capacity of water,θ is the temperature in the overlaying atmospheric box, D_u is the depth of the upper ocean box, D_{si} is the thickness of an optional layer of sea ice and γ the insolation effect of this layer. f_{ow} and f_{si} are respectively the fractions of surface area of open water and of sea ice with $f_{ow} = 1 - f_{si}$. The time scale τ is chosen to accommodate an ocean-atmosphere heat transport of about 2.3 PW during interglacial periods (Gildor and Tziperman, 2001) [13]. This equation greatly simplifies as we disregard sea ice in our study with this model, so the term within square brackets equals 1. The atmosphere-ocean salinity flux $Q_{S,a}$ is dictated by the precipation P and evaporation E;

$$Q_{S,a} = -\big(P - E\big)S_0, \tag{4.18}$$

with S_0 a reference salinity.

4.4 Bio-geochemistry model

The bio-geochemistry model includes total CO_2 ($\sum CO_2$) and alkalinity (A_T) as prognostic variables which are used to calculate pCO_2. PO_4 is used as a limiting nutrient in this model; this allows for the disregarding of the complex interactions the complete nitrogen cycle introduces (Maier-Reimer, 1993) [23]. This model is of the closed-system type (Sigman and Boyle, 2000) [32], which implies that A_T and total PO_4 are constant and only the distribution through the ocean changes. Surface pCO_2 is calculated from $\sum CO_2$, alkalinity, salinity, temperature, according to Yamanaka (1996) [42]. The equations for $\sum CO_2$, A_T and PO_4 are identical to those for T and S apart from an extra source/sink term, i.e.

$$\frac{\partial i}{\partial t} + \frac{\partial}{\partial y}(vi) + \frac{\partial}{\partial z}(wi) = K_{\mathrm{h}}\frac{\partial i}{\partial y} + K_{\mathrm{v}}\frac{\partial i}{\partial z} + S_i, \tag{4.19}$$

where we used i as a placeholder for the different tracers. The source/sink term is different for each variable, and below we will discuss the included processes. The ratio P:N:C is assumed constant at 1:16:122 in particulate organic matter. We denote the ratio P:N as R_N and the ratio P:C as R_C.

The rate of export production per box, EP (the part of organic matter that is produced in the surface boxes and sinks as particulate organic flux), depends on the latitude of the box (via the light factor), the amount of PO_4 and the ocean area not covered by sea ice, A_{ow}, i.e.

$$\mathrm{EP} = r_b L_f [\mathrm{PO_4}] A_{ow}, \tag{4.20}$$

where L_f is the light factor taken to be the average solar radiation in each box and $[PO_4]$ the phosphate concentration in each box. r_b is a tuning parameter which can be used to implicitly take into account other factors affecting the production, like a lack of iron, and thus differs for each box. We define the rain ratio (RR) as by Maier-Reimer (1993) [23];

$$\mathrm{RR} = 61 \exp\left(0.1(T - 10)\right), \tag{4.21}$$

with T the surface temperature. This rain ratio dictates the ratio of organic to inorganic carbon atoms from the total ΣCO_2 per PO_4 molecule that sinks as particulate flux.

Export production of organic soft tissue and calcite shells reduces the total CO_2 at the surface at rates of $R_C \times$EP and RR$\times$EP respectively, and through the process of remineralisation the total CO_2 is increased in the deep ocean boxes at these same rates. Secondly, the total CO_2 is affected by the gas exchange between the atmosphere and the upper ocean. The flux between the ocean and atmosphere is linear in the pCO_2 difference between the atmosphere and surface ocean boxes;

$$F_{CO_2} = \mathrm{PV}\big([\mathrm{CO_{2,a}}] - [\mathrm{CO_{2,o}}]\big)A_{ow}, \tag{4.22}$$

where PV is the piston velocity (Siegenthaler and Sarmiento, 1993) [31]. Hence, for the surface ocean boxes the ΣCO_2 source/sink term is given as

$$\begin{aligned} S_{\Sigma \mathrm{CO_2}} = -R_C \times \mathrm{EP} - \mathrm{RR} \times \mathrm{EP} + \\ \mathrm{PV}\big([\mathrm{CO_{2,a}}] - [\mathrm{CO_{2,o}}]\big)A_{ow}, \end{aligned} \tag{4.23}$$

and for the deep ocean boxes we have

$$S_{\Sigma \mathrm{CO_2}} = R_C \times \mathrm{EP} + \mathrm{RR} \times \mathrm{EP}. \tag{4.24}$$

Production of calcite shells at the surface reduces the alkalinity of the surface boxes at a rate of 2$\times$RR$\times$EP while dissolution of these shells in the deep ocean increases the alkalinity at the very same rate. The export production of soft tissue increases alkalinity at the surface boxes at a rate of $R_N \times$EP and remineralisation in the deep ocean decreases it at the same rate. For a surface ocean box the source/sink term takes the form of

$$S_{A_T} = -2 \times \mathrm{RR} \times \mathrm{EP} + R_N \times \mathrm{EP}, \tag{4.25}$$

and for a deep ocean box

$$S_{A_T} = 2 \times \mathrm{RR} \times \mathrm{EP} - R_N \times \mathrm{EP}. \tag{4.26}$$

Lastly, for the phosphate, export production at the surface and remineralisation in the deep ocean act as a sink and source respectively, at a rate of EP. Thus

$$S_{\mathrm{PO_4}} = \mp \mathrm{EP}, \tag{4.27}$$

where the minus (plus) sign corresponds with the surface (deep) boxes.

4.5 Milanković module

The Milanković cycles are incorporated in the calculation of the insolation per box, following the model as

Table 4.1: Parameters modified or added by Tigchelaar (2011) [36] with respect to Gildor et al. (2002) [14].

Parameter, Unit	Description	Original Value	Eocene Value
f_{L1},..., f_{L4}	land fraction	0.5, 0.2, 0.35, 0.5	0.21, 0.19, 0.30, 0.57
$K_{\mathrm{h,up}}$ [$\mathrm{m^2\ s^{-1}}$]	surface horizontal diffusion coefficient	6.0×10^{-4}	1.5×10^{-4}
$K_{\mathrm{h,deep}}$ [$\mathrm{m^2\ s^{-1}}$]	deep horizontal diffusion coefficient	7.5×10^{-3}	2.0×10^{-3}
K_{v} [$\mathrm{m\ s^{-1}}$]	vertical mixing coefficient	7.0×10^{-8}	4.5×10^{-8}
r [$\mathrm{s^{-1}}$]	friction coefficient	3.0×10^{-4}	4.2×10^{-8}
K_θ [$\mathrm{s^{-1}\ K^{-2}}$]	atmospheric heat transport coefficient	15.5×10^{20}	13.5×10^{20}
P_{lw1},..., P_{lw4}	atmospheric emissivity	0.61, 0.49, 0.52, 0.67	0.62, 0.53, 0.51, 0.70
$\mathrm{CO_{2,in}}$ [ppm]	$p\mathrm{CO_2}$	320	1500
δ_{ice} [‰]	isotopic composition of ice		−35
${V_{\mathrm{W}}}^0$ [$\mathrm{m^3}$]	volume Eocene ocean		1.3×10^{18}
${\delta_{\mathrm{W}}}^0$ [‰]	δ_{W} Eocene ocean		0.244
$I\,S_{\max}$ [$\mathrm{m^3}$]	maximum volume Antarctic ice sheet	9×10^{16}	2.57×10^{16}

proposed by Berger (1978) [1]. Fourier analysis of the solar insolation arising from this model as presented in Fig. 4.2 reveals the relevant frequencies to be present. Besides having effect on the total energy balance through the insolation, the Milanković forcing also affects the biogeochemical production via the light factor L_f and is incorporated as a sink term in the land ice model.

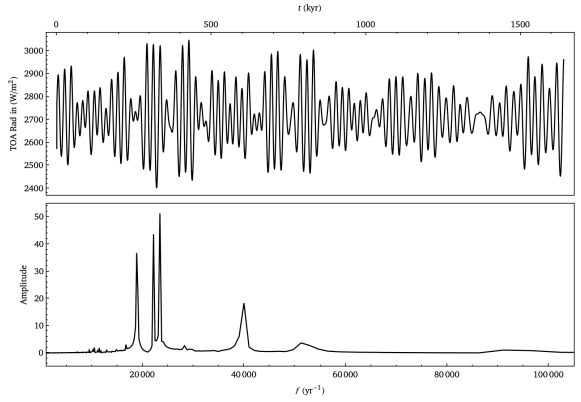

Fig. 4.2: Time evolution (top) and Fourier spectrum (bottom) of insolation as modulated by the Berger model.

4.6 $_{18}$O isotope module

An additional module was added by Tigchelaar et al. (2011) [36] to compute variations in $\delta^{18}\mathrm{O}$. The oxygen isotopic composition of sea-water, δ_{w} is calculated from changes in land ice and ocean volume combined with conservation of total $\delta^{18}\mathrm{O}$;

$$V_{\mathrm{w}}^0 \times \delta_{\mathrm{w}} = V_{\mathrm{ice}} \times \delta_{\mathrm{ice}} + V_{\mathrm{w}} \times \delta_{\mathrm{w}}, \qquad (4.28)$$

where V_{w}^0 is the volume of the Eocene ocean, and V_{w} is the volume of the ocean after land ice formation, i.e. $V_{\mathrm{w}} = V_{\mathrm{w}}^0 - V_{\mathrm{ice}}$. δ_{ice} is the oxygen isotopic composition of land ice and δ_{w}^0 (δ_{w}) the Eocene ocean isotopic composition before (after) land ice formation. The values used for these variables can be found in Table 4.1. Following the calcite-temperature relation of Shackleton (1974) [30], we compute the calcite isotopic composition δ_{c} from the sea-water isotopic composition δ_{w} and the simulated temperature T (in °C) of the deep ocean boxes as

$$T = 16.9 - 4.38(\delta_{\mathrm{c}} - \delta_{\mathrm{w}}) + 0.1(\delta_{\mathrm{c}} - \delta_{\mathrm{w}})^2. \qquad (4.29)$$

The initial value δ_{w}^0 was chosen such that the modelled Eocene deep sea temperature matches the measured late Eocene calcite isotopic composition.

4.7 Eocene reference state

The parameter values defining the climate system in the model can be changed to resemble the Eocene climatic boundary conditions. The adapted parameters, as they were used in Tigchelaar et al. (2011) [36], are displayed in Table 4.1. The representative land fractions were originally obtained from Markwick et al. (2000) [24]. Tigchelaar et al. (2011) [36] Sec. 3.1 comprises an extensive comparison of this modelled climate with proxy data, finding that this is not a perfect representation of the Eocene climate, partly due to known shortcomings of climate box models. In this study however, the details are of limited importance, as our primary focus is the global reflection of the tipping mechanisms as introduced by an SPP-TH overturning transition. Lastly, in this present model study we disregard sea ice as noted earlier. This is because of the fact that this specific model, as many other models, suffers from a too high sensitivity to the sea ice albedo feedback, resulting in oceans potentially becoming completely sea ice covered. Also, in studying the inception of the Antarctic ice sheet on a warm Earth, sea ice is deemed to initially only play a minor role, making the disregard of it a safe assumption for now. As noted earlier, throughout this study we will vary T_{melt} for the Southern polar box, to control the inception of an Antarctic land ice sheet.

5 Results

5.1 Transition between overturning states

A simulation run lasting 1.0 Myr is executed in which the climate system settles into an SPP overturning equilibrium. Following this, the system is run for 20,000 years to let it adapt to an active bio-geochemistry and adjusted parameter values.

In Dekker et al. (2018) [7], K_v is tuned with respect to Tigchelaar et al. (2011) [36] to facilitate that the atmospheric pCO_2 decreases down to roughly 800 ppm by the change in overturning state. This choice was made to be in accordance with other model studies by DeConto and Pollard (2003) [6] where ice growth was found to be possible below this concentration, and resulted in $K_v = 1 \times 10^{-9}$ m^2 s^{-1} being used for this study. However, this means that the atmospheric pCO_2 would almost decrease by half merely due to the change in overturning state; a step of a magnitude that seems unlikely and, as we will see, is not a necessity for a scenario with ice inception at a realistic T_{melt} within this specific model. Hence, in this study we retain $K_v = 4.5 \times 10^{-8}$ m^2 s^{-1} as in Tigchelaar et al. (2011) [36].

After initialisation, a 100-day-long density perturbation (1030 kg m^{-3}) is applied to the upper northern hemispheric polar ocean box. This perturbation forces a transition from the SPP to the TH overturning state (Fig. 5.1). From the SPP to the TH overturning state, vertical transport in the northern polar ocean box is initiated and vertical transport in the southern polar box decreases.

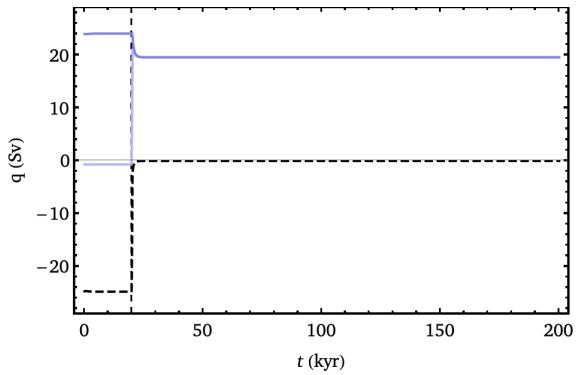

Fig. 5.1: Development of the vertical transport in the northern and southern polar box (resp. in turquoise and blue) following a density perturbation, for a run with no ice inception. Difference $q_N - q_S$ in black. Vertical dashed line indicates start of density perturbation (1030 kg m^{-3} in upper northern hemispheric polar ocean box).

In Fig. 5.4 we see further substantiation of the aforementioned characteristics which we also discussed in Sec. 2.2 and in Fig. 5.2 we display the effects of active biogeochemistry. Looking ahead qualitatively at the direct effects of the SPP-TH transition in a case with no ice inception and with active biogeochemistry (Fig. 5.4), it is apparent that a transition from an SPP overturning to a TH overturning state results in a considerable temperature increase in both the northern polar atmospheric and upper ocean box. This is partly due to the fact that, in contrast to the SPP overturning state, in the TH overturning state there is no upwelling from the northern polar deep ocean box cooling the overlaying boxes, and instead warmer water is transported from the northern equatorial upper ocean box. In all other boxes, average temperatures decrease; this is presumably a consequence of the redistribution of energy in the system relative to the SPP overturning state, and the fact that in the TH overturning Southern sinking is weakened relative to the SPP overturning, resulting in less warm water being transported towards the polar box.

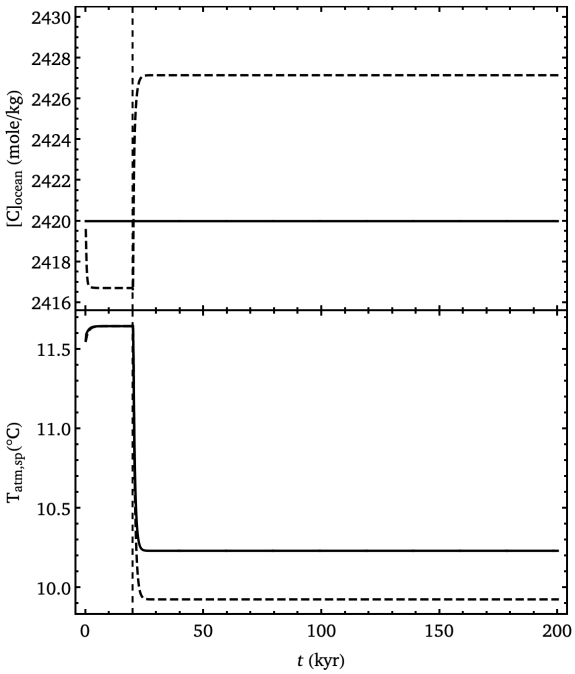

Fig. 5.2: The evolution of the total carbon content of the ocean and the atmospheric temperature in the southern polar box. Inactive (active) biochemistry in (dashed) black. Run with no ice inception.

In the case with active biogeochemistry relative to the case without active biochemistry, there is a second component to the change in atmospheric temperature. This second part of the temperature decrease is caused by a decrease in the atmospheric pCO_2 as a result of the changed biogeochemical equilibrium. The total carbon content of the ocean increases from ~2417 mole/kg up to ~2427 mole/kg, acting as a sink facilitating an atmospheric pCO_2 decrease from ~1530 ppm to ~1435 ppm. In this study, the net effect of this pCO_2 decrease is only

around 0.3 °C however.

Note that this is in stark contradiction with Tigchelaar et al. (2011) [36], where the atmospheric pCO_2 decrease is coined as the driving factor of cooling and ice inception. For this choice of K_v in this specific model study, the direct temperature effect of the overturning strength is the dominant driving factor of the climate transition and the effect of the atmospheric pCO_2 decrease as a result of the active biochemistry is of negligible magnitude. Indeed, when we estimate the temperature decrease resulting from the observed pCO_2 decrease using the contemporary accepted climate sensitivity of $\sim$ 3.0 °C per instant pCO_2 doubling, i.e.

$$\Delta T = 4.33 \ln \frac{[CO_2]}{[CO_2]_0}, \tag{5.1}$$

we find

$$\Delta T = 4.33 \ln \frac{1435 \text{ ppm}}{1530 \text{ ppm}} \approx -0.28 \text{ °C}, \tag{5.2}$$

which is in agreement with the order of magnitude found in the model study.

5.2 Cascading transitions

We run the described simulation for a range of $\{T_{\text{melt}} \in \mathbb{R} \mid 274 \text{ K} \leq T_{\text{melt}} \leq 280 \text{ K}\}$. We consider 280 K to be a realistic upper bound for the box-averaged southern polar atmosphere temperature for which ice growth could still initiate.

There are three distinct scenarios that can be discerned:

1. Subcritical scenario: The atmospheric temperature decrease as a result of the transition in the ocean overturning is not sufficient to initiate ice growth.

2. Supercritical scenario: The atmospheric temperature decrease as a result of the transition in the ocean overturning is sufficient to initiate ice growth. Ice volume stabilises at the maximum allowed volume.

3. Critical scenario: The atmospheric temperature decrease as a result of the transition in the ocean overturning is sufficient to initiate ice growth, but the resulting ice volume is approximately a factor 10^6 smaller than the maximum allowed ice volume, and disappears seasonally.

Additionally, we found a case closely related to the critical scenario where the ice volume is still very small, but is stable throughout the year. It is assumed that this amount of ice is not yet sufficient to initiate the feedback mechanisms that would allow further growth.

5.2.1 Subcritical transition

In this scenario, the atmospheric temperature decrease as a result of the transition in the ocean overturning is not sufficient to initiate ice growth. This scenario is encountered for $T_{\text{melt}} = 277.5$ K and presented in Fig. 5.4. The box-averaged southern polar atmosphere temperature decreases to $\sim$ 9.9 °C, just above the critical temperature. Atmospheric pCO_2 decreases from $\sim$ 1500 ppm to $\sim$ 1435 ppm due to the adjusting biochemical equilibrium. As already noted in Section 5.1, the Northern polar atmospheric temperature is increased considerably in the TH overturning state with respect to the SPP overturning. Atmospheric temperatures in all other boxes decrease. In the $\delta^{18}O$ profile we observe a single step of increase, where it increases from $\sim$ 1.10‰ up to $\sim$ 1.56‰ within the span of $\sim$ 5 kyr.

5.2.2 Supercritical transition

In this scenario, encountered for $T_{\text{melt}} = 277.9$ K (Fig. 5.5), the atmospheric temperature decrease as a result of the transition in the ocean overturning is sufficient to initiate ice growth. The initial reaction of the climate system to the overturning transition is identical to the subcritical transition, but additional effects are introduced by the inception of the Antarctic ice sheet. Most notably, an increase in the vertical transport in the Southern polar ocean is observed; this can be explained by the fact that due to Antarctic ice inception the Southern polar-equatorial ocean temperature difference increases relative to the case without ice inception, strengthening the surface flow towards the pole. Furthermore, this is accompanied by a decrease in the Southern polar-equatorial salinity difference aided by an increase in local Southern polar evaporation, also effectively strengthening the surface flow towards the pole. Furthermore, the atmospheric pCO_2 decreases in an additional slow step down to $\sim$ 1415 ppm. The atmospheric temperatures in all boxes decrease slightly further relative to the subcritical transition, but the decrease is most pronounced in the Southern polar box where it stabilises at $\sim$ 8.5 °C. This decrease can be attributed to the albedo effect of the increasing land surface which is covered by land ice. Finally, in the $\delta^{18}O$ profile we observe a distinct two-step evolution, where in addition to the first step caused by the overturning transition, the $\delta^{18}O$ increases a further $\sim$ 0.92‰ up to $\sim$ 2.48‰ over the course of ~80 kyr. The combined magnitude of both steps is $\sim$ 1.56‰, which is in reasonable accordance to the observed $1.2 - 1.5$‰ change that is observed at the Eocene-Oligocene boundary. Note however the lack of a distinct plateau between the two steps; such behaviour is deemed unlikely to be intrinsic to the overturning-ice coupled dynamical system itself in this specific model, and is more probably attributed to external forcings which we will discuss in Section 5.3.

5.2.3 Critical transition

In this scenario, encountered at $T_{\text{melt}} = 277.8$ K, the atmospheric temperature decrease as a result of the transition in the ocean overturning is sufficient to initiate ice

growth, but the resulting ice volume is approximately an order 6 smaller than the maximum allowed ice volume, and disappears seasonally. Concerning the reaction of climate system this case is identical to the subcritical transition, so it is assumed that the seasonal nature of the ice inhibits the feedback processes which would let the climate settle into its consistently fully glaciated state. In this study, a scenario as such is most interesting in the context of delayed full glaciation due to external forcing, which would pose a possible explanation for the plateau in the δ^{18}O profile.

5.3 Effects of Milanković forcing

We study the effect of variability in the insolation on the climate system using the Milanković cycle module available in the Gildor-Tziperman model. This module is based on the Berger model, and is originally meant to represent the last 5 Myr before present. However, under the assumption that the periodicity and amplitudes of orbital variations are equally applicable to the Eocene-Oligocene boundary, we use it here to approximate the effects this periodic forcing would have on the climate system. As noted in Sec. 4.5, in this model the Milanković forcing is incorporated in the atmospheric energy balance, as a sink for the land ice and in the biochemical production.

In Fig. 5.3 we present a model run with $T_{\text{melt}} = 277.9$K where we implemented the Milanković forcing. Apparent is that the variability in insolation has the potential to delay the onset of ice inception, and with that the second step of the two step mechanism. Simulations executed with different phases of the Milankovic forcing delayed or advanced the second step on differing time scales. The introduction of noise to the system unavoidably reduces the distinctness of the cascaded transition, but coincidentally[1] the simulation shown in Fig. 5.3 finds the duration of the second step to be considerably closer to the ~ 40 kyr observed in proxy data.

At present, we did not explicitly find scenarios where with active Milanković forcing ice inception occurred where it would not have occurred were it inactive, but considering the nature of fold bifurcating systems such scenarios should equally well exist.

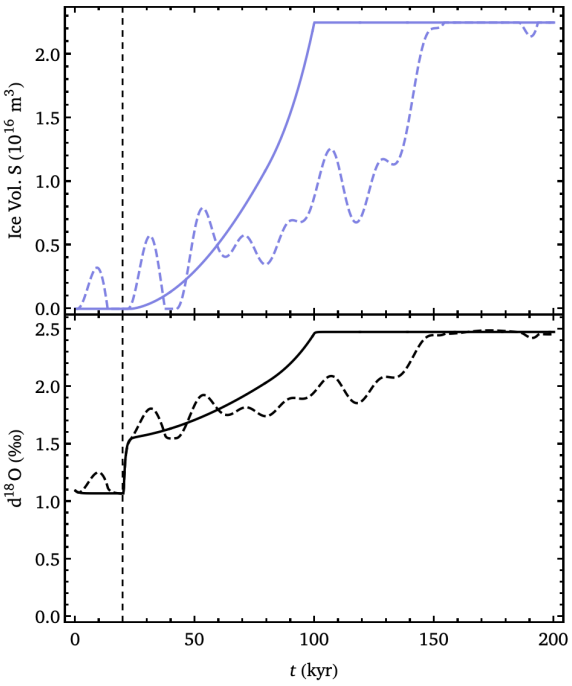

Fig. 5.3: Evolution of Southern hemispheric ice volume (top panel) and δ^{18}O (bottom panel) following SPP-TH transition. Run for $T_{\text{melt}} = 277.9$K, (in)active Milankovic forcing denoted as dashed (solid).

[1] and presumably not more than that.

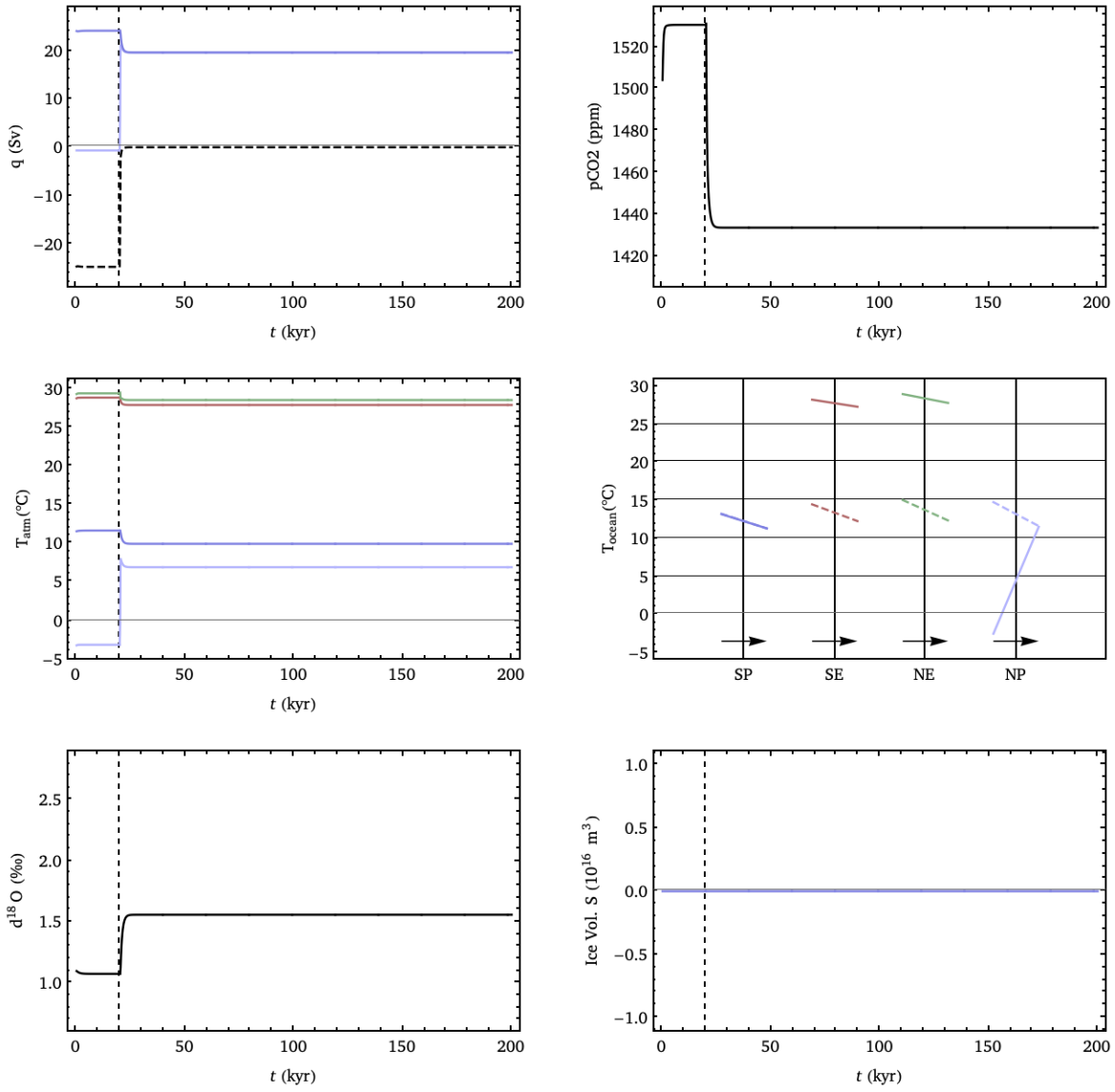

Fig. 5.4: From top left to bottom right: Development of 1) the vertical transport in the northern and southern polar box (resp. in turquoise and blue) and difference $q_N - q_S$ in black, 2) atmospheric pCO_2, 3) average atmospheric box temperatures, turquoise/blue for Northern/Southern polar boxes and green/red for Northern/Southern equatorial boxes, 4) average ocean box temperatures before and after the transition (arrows indicate direction SPP to TH), solid/dashed denotes surface/deep ocean, 5) $d^{18}O$ and 6) Southern hemispheric land ice volume. Vertical dashed line indicates start of density perturbation. Simulation run for subcritical transition at $T_{\text{melt}} = 277.5$ K.

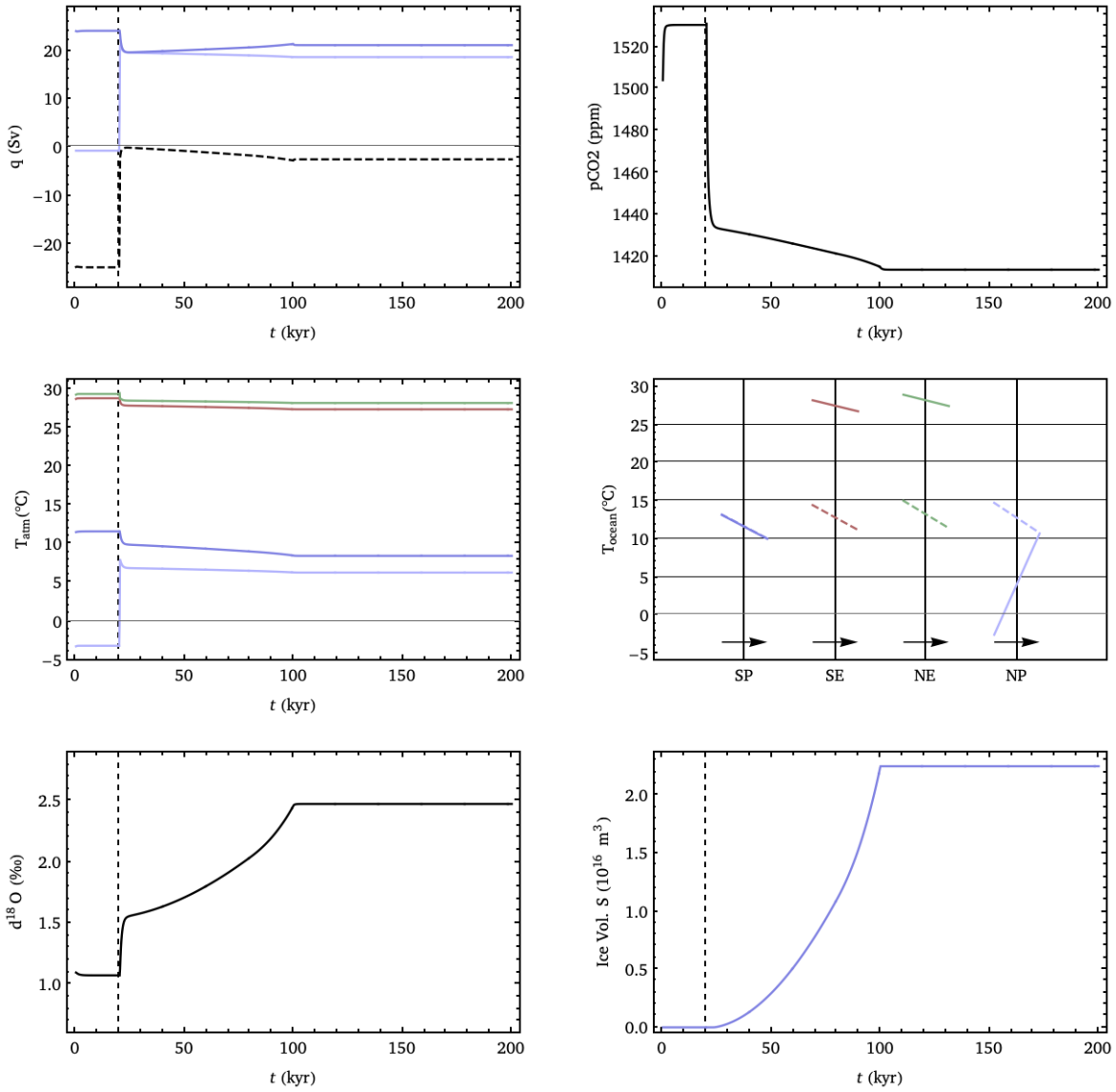

Fig. 5.5: From top left to bottom right: Development of 1) the vertical transport in the northern and southern polar box (resp. in turquoise and blue) and difference $q_N - q_S$ in black, 2) atmospheric pCO_2, 3) average atmospheric box temperatures, turquoise/blue for Northern/Southern polar boxes and green/red for Northern/Southern equatorial boxes, 4) average ocean box temperatures before and after the transition (arrows indicate direction SPP to TH), solid/dashed denotes surface/deep ocean, 5) $d^{18}O$ and 6) Southern hemispheric land ice volume. Vertical dashed line indicates start of density perturbation. Simulation run for supercritical transition at $T_{\text{melt}} = 277.9$ K.

6 Conclusion

In this thesis, we applied the concepts of cascading tipping events to the Eocene-Oligocene transition in an attempt to describe it as such, where a transition in ocean overturning circulation could induce a temperature drop sufficient to initiate Antarctic land ice inception. We studied the individual bifurcating behaviour of the ocean and land ice system, and argued that they exhibit characteristics comparable to the elementary coupled fold-fold bifurcating system as presented in Dekker et al. (2018) [7]. We presented a rudimentary linear coupling between the two systems to show the viability of such an interpretation, however for a more robust model a dynamically modelled atmosphere is a necessity.

Using the 4+8-box Gildor-Tziperman climate model we studied the effect of the SPP-TH overturning transition in a holistic manner, and found that for realistic T_{melt} there can exist scenarios where the climate system undergoes a two-step cascaded tipping event as just described. The combined magnitude of the δ^{18}O steps was found to be $\sim 1.56‰$, which is in reasonable accordance to the observed $1.2-1.5‰$ change that is observed at the Eocene-Oligocene boundary. In contradiction to Tigchelaar et al. (2011) [36], the driving force of this cascaded tipping is found not to be the change in atmospheric pCO_2 due to an adjusted biogeochemical equilibrium, but merely the change in temperature due to changed vertical transport in the ocean is sufficient to initiated such a transition. We found that in this particular model study the 200 kyr plateau as observed in proxy data is not intrinsic to the cascaded tipping mechanism itself, but we argue it can potentially be introduced by stochastic noise or in our simulation the Milanković forcing. This model study failed to correctly reflect the duration of the first step due to the overturning transition, but under the influence of the Milanković forcing, the duration of the second step due to land ice inception is found within the right order of magnitude. An array of mechanisms not included in this simple model might delay or extent either of the two steps, so quantitative conclusions on this should be made with caution and will not be made here.

Further research

The exclusion of sea ice in this present study proved problematic when Southern ice volume approached the maximum allowed volume. Further ice growth was simply cut off here, inhibiting realistic behaviour in these regimes. The inclusion of sea ice in further study would in all probability allow study of the system evolution beyond the limit we encountered here.

Furthermore, we deem there is value in more thorough quantitative study of the effects of the Milanković forcing, possibly using the full numerical solution (Laskar et al., 2004) [19], considering the effect of varying amplitude of this forcing. In addition to the phase of the Milanković forcing, the amplitude of the forcing is expected to significantly affect the precise bifurcating behaviour of the climate system.

Outlook

To conclusively answer the question "can we explain the Eocene-Oligocene transition as a cascading tipping event?", I would say that the mechanism presented in this thesis does certainly qualify as a potential explanation. Modelling the exact timescales and magnitudes of the individual steps remains a challenge, and even within more sophisticated 3D models these would be subject to the approximations and parameterizations made within such models. Nevertheless, it would be valuable to study this cascading behaviour in more complex models, to see how this behaviour holds up in a climate system of higher detail, and possibly finding hints to other dynamics which might also exhibit a cascading tipping event. Such 3D models could include the full ocean dynamics, including an Antarctic Circumpolar Current, and potentially a more realistic land/sea ice model than was used here. Tectonic changes like the subsidence of the Greenland-Scotland ridge and/or the opening of the Tasman Gateway and Drake Passage could introduce additional forcing of the system, but all this can still fit inside the framework discussed in this thesis. The cascading interaction between the ocean overturning and land ice as presented might not be the complete explanation of the transition, but given the physical rigidity of this interaction, it might at least be a part of the solution.

Acknowledgements

First and foremost I want to thank Dr. Anna von der Heydt for her supervision and guidance during this thesis. I genuinely enjoyed our easy-going but fruitful meetings and our bilateral enthusiasm for the subject kept me fully motivated throughout. It was a joy to see these meetings evolve from mostly answering questions to discussions on equal terms. Secondly I would like to thank Henk Dijkstra and Rik Spijkers for the two joint meetings we had, which allowed for different viewpoints and new inspiration. Lastly, I thank my family and Karlijn Ploeg, for supporting me, supplying me with constructive critique, questioning me, as only an Earth scientist can question a physicist, and letting me draw a lot of bifurcation diagrams trying to explain what they are.

References

[1] Berger, A. L.: Long-Term Variations of Daily Insolation and Quaternary Climatic Changes, Journal of the Atmospheric Sciences, Vol. 35, 2362-2367, 1978.

[2] Coxall, H. K., Pearson, P. N.: The Eocene-Oligocene Transition, in Deep-Time Perspectives on Climate Change: Marrying the Signal from Computer Models and Biological Proxies, edited by: Williams, M., Haywood, A. M., Gregory, F. J., and Schmidt, D. N., 351-387, The Micropalaeontological Society Special Publication, 2007.

[3] Coxall, H. K., Wilson, P. A., Pälike, H., Lear, C. H., and Backman, J.: Rapid stepwise onset of Antarctic glaciation and deeper calcite compensation in the Pacific Ocean, Nature, 433, 53-57, 2005.

[4] Cramer, B. S., Toggweiler, J. R., Wright, J. D., Katz, M. E., and Miller, K. G.: Ocean overturning since the Late Cretaceous: Inferences from a new benthic foraminiferal isotope compilation, Paleoceanography, 24, PA4216, 2009.

[5] Davies, R., Cartwright, J., Pike, J., and Line, C.: Early Oligocene Initiation of North Atlantic Deep Water Formation, Nature, 410, 917-920, 2001.

[6] Deconto, R., and Pollard, D.: Rapid Cenozoic glaciation of Antarctica induced by declining atmospheric CO_2, Nature, 421, 245-249, 2003.

[7] Dekker, M. M., Heydt, A. S. von der, and Dijkstra, H. A.: Cascading transitions in the climate system, Earth Syst. Dynam., 9, 1243-1260, 2018.

[8] Dijkstra, H. A., and Weijer, W.: Stability of the global ocean circulation: The connection of equilibria within a hierarchy of models, Journal of Marine Research, 61, 725-743, 2003.

[9] Dijkstra, H. A., and Weijer, W.: Stability of the global ocean circulation: basic bifurcation diagrams, Journal of Physical Oceanography, 35, 933-948, 2005.

[10] Dockery, D. and Lozouet, P.: Biotic patterns in Eocene-Oligocene Molluscs of the Atlantic Coastal Plain, USA, in: From Greenhouse to Icehouse, edited by: Prothero, D. R., Ivany, L., and Nesbitt, E. A., 303-340, Columbia University Press, 2003.

[11] Eldrett, J. S., Greenwood, D. R., Harding, I. C., and Huber, M.: Increased seasonality through the Eocene to Oligocene transition in northern high latitudes, Nature, 459, 176-179, 2007.

[12] Gildor, H., and Tziperman, E.: Sea ice as the glacial cycles' Climate switch: role of seasonal and orbital forcing, Paleoceanography, 15, 605-615, 2000.

[13] Gildor, H., and Tziperman, E.: A sea ice climate switch mechanism for the 100-kyr glacial cycles, Journal of Geophysical Research, Vol. 106, No. C5, 9117-9133, 2001.

[14] Gildor, H., Tziperman, E., and Toggweiler, J. R.: Sea ice switch mechanism and glacial-interglacial CO_2 variations, Global Biochemical Cycles, Vol. 16, No. 3, 6.1-6.13, 2002.

[15] Hays, J. D., Imbrie, J., and Shackleton, N. J.: Variations in the Earth's Orbit: Pacemaker of the Ice Ages, Science, 194, 1121-1132, 1976.

[16] Haywood, A., Valdes, P., Lunt, D., and Pekar, S.: The Eocene-Oligocene boundary and the Antarctic Circumpolar Current, Geophysical Research Abstracts, vol. 12, pp. EGU2010-5031, 2010.

[17] Heydt, A. S. von der, and Ashwin, P.: State-dependence of climate sensitivity: attractor constraints and palaeoclimate regimes, 2018.

[18] Ivanovic, R. F., Gregoire, L. J., Wickert, A. D., Valdes, P. J., and Burke, A.: Collapse of the North American ice saddle 14,500 years ago caused widespread cooling and reduced ocean overturning circulation. Geophys. Res. Lett., 44, 383-392, 2017.

[19] Laskar, J., Robutel, P., Joutel, F., Gastineau, M., Correia, A. C. M., and Levrard, B.: A long-term numerical solution for the insolation quantities of the Earth, A&A, 428, 261-285, 2004.

[20] Lear, C. H., Elderfield, H., and Wilson, P. A.: Cenozoic deep- sea temperatures and global ice volumes from Mg/Ca in benthic foraminiferal calcite, Science, 287, 269-272, 2000.

[21] Liu, Z., Pagani, M., Zinniker, D., DeConto, R., Huber, M., Brinkhuis, H., Shah, S. R., Leckie, R. M., and Pearson, A.: Global cooling during the Eocene-Oligocene climate transition, Science, 323, 1187-1190, 2009.

[22] Livermore, R., Nankivell, A., Eagles, G., and Morris, P.: Paleogene opening of Drake passage, Earth Planet. Sc. Lett., 236, 459-470, 2005.

[23] Maier-Reimer, E.: Geochemical cycles in an ocean general circulation model: Preindustrial tracer distribution, Global Biogeochem. Cycles, 7, 645-677, 1993.

[24] Markwick, P. J., Rowley, D. B., Ziegler, A. M., Hulver, M. L., Valdes, P. J., and Sellwood, B. W.: Late Cretaceous and Cenozoic global palaeogeographies: Mapping the transition from a "hot-house" to an "ice-house" world, GFF, 122, 103, 2000.

[25] McManus, J. F., Francois, R., Gherardi, J. M., Keigwin, L. D., and Brown-Leger, S.: Collapse and rapid resumption of Atlantic meridional circulation linked to deglacial climate changes, Nature, 428, 834-837, 2004.

[26] Mikkelsen, T. B., Grinsted, A., and Ditlevsen, P.: Influence of temperature fluctuations on equilibrium ice sheet volume, The Cryosphere, 12, 39-47, 2018.

[27] Oerlemans, J.: A quasi-analytical ice-sheet model for climate studies, Nonlinear Processes in Geophysics, 10, 441-452, 2003.

[28] Rohde, R. A.: Milankovitch Variations. Own work. Released under Creative Commons Attribution-ShareAlike 3.0. Unported, 2006.

[29] Scher, H. D. and Martin, E. E.: Timing and climatic consequences of the opening of Drake passage, Science, 312, 428-430, 2006.

[30] Shackleton, N. J.: Attainment of isotopic equilibrium between ocean water and the benthonic foraminifera genus Uvigerina: isotopic changes in the ocean during the last glacial, C. N. R. S. Colloq., 219, 203-209, 1974.

[31] Siegenthaler, U., and Sarmiento, J.: Atmospheric carbon dioxide and the ocean, Nature, 365, 119-125, 1993.

[32] Sigman, D. M., and Boyle, E. A.: Glacial/interglacial variations in atmospheric carbon dioxide, Nature, 407, 859-869, 2000.

[33] Sijp, W. P. and England, M. H.: Effect of the Drake Passage throughflow on global climate, J. Phys. Oceanogr., 34, 1254-1266, 2004.

[34] Sijp, W. P., England, M. H., and Toggweiler, J. R.: Effect of Ocean Gateway Changes under Greenhouse Warmth, J. Climate, 22, 6639-6652, 2009.

[35] Stommel, H.: Thermohaline Convection with Two Stable Regimes of Flow, Tellus, 13, 224-230, 1961.

[36] Tigchelaar, M., Heydt, A. S. von der, and Dijkstra, H. A.: A new mechanism for the two-step δ^{18}O signal at the Eocene-Oligocene boundary, Clim. Past, 7, 235-247, 2011.

[37] Thomas, D. J., Bralower, T. J., and Jones, C. E.: Neodymium isotopic reconstruction of late Paleocene-early Eocene thermohaline circulation, Earth Planet. Sc. Lett., 209, 309-322, 2003.

[38] Thomas, D. J.: Evidence for deep-water production in the North Pacific Ocean during the early Cenozoic warm interval, Nature, 430, 65-68, 2004.

[39] UNESCO. 10th report of the joint panel on oceanographic tables and standards. Technical Report 36, UNESCO Tech. Pap. in Mar. Sci., 1981.

[40] Via, R. K. and Thomas, D. J.: Evolution of Atlantic thermohaline circulation: Early Oligocene onset of deep-water production in the North Atlantic, Geology, 34, 441-444, 2006.

[41] Welander, P.: Thermohaline effects in the ocean circulation and related simple models, *in* Large-Scale Transport Processes in Oceans and Atmosphere, J. Willebrand and D.L.T. Anderson, eds., D. Reidel, 163-200, 1986.

[42] Yamanaka, Y.: Development of ocean biochemical general circulation model, Tech. Rep. 1, Cent. for Clim. Sys. Res., Univ. of Tokyo, Tokyo, 1996.

[43] Zachos, J. C., and Kump, L. R.: Carbon cycle feedbacks and initiation of Antarctic glaciation in the earliest Oligocene, Global Planet. Change, 47, 51-66, 2005.

[44] Zachos, J. C., Quinn, T. M., and Salamy, K. A.: High-resolution (10^4 years) deep-sea foraminiferal stable isotope records of the Eocene-Oligocene climate transition, Paleoceanography, 11, 251-266, 1996.

Appendices

A Proofs concerning bifurcations

Lemma A.1 *For $a_1 < 0$, the system X from Eq. 1.1 has two equilibria at $X' = -\sqrt{-a_1}$ and $X' = \sqrt{-a_1}$, of which the first is stable and the latter unstable.*

Proof: We write $X = X' + \delta X$, where X' is a steady state and δX a small perturbation around this state such that $X' \gg \delta X$. Substituting this identity we find

$$\frac{dX'}{dt} + \frac{d\delta X}{dt} = a_1 + \left(X' + \delta X\right)^2 = a_1 + \left(X'^2 + X'\delta X + \delta X^2\right), \tag{A.1}$$

which upon neglecting the product of perturbations and identifying $dX'/dt = a_1 + X'^2$ yields

$$\frac{d\delta X}{dt} = X'\delta X. \tag{A.2}$$

For $\delta X > 0$, a negative derivative, as a consequence of substituting $X' = -\sqrt{-a_1}$, implies convergence to that steady state, and thus stability. A positive derivative, as a consequence of substituting $X' = \sqrt{-a_1}$, implies diversion of the perturbation from the steady state, and thus instability. For $\delta X < 0$ the signs of all relations must be opposite, which is readily facilitated by the change of sign in δX.

Lemma A.2 *The system X in Eq. 1.2 has only one stable equilibrium at a maximum when $a_1 > 0$.*

Proof: As Eq. 1.2 is a third degree polynomial, by induction we know it has a maximum of three roots, for $a_1 \neq 0$. The roots resemble equilibria of the system, which are stable if and only if $\dot{X}(X' + \delta X) < 0$ and $\dot{X}(X' - \delta X) > 0$ for $X' \gg \delta X$. Assuming $a_1 > 0$, and one singular equilibrium at $X = X_0$ we know that $\dot{X}(-\infty) \to -\infty$; indicating $\dot{X}(X' - \delta X) < 0$, hence X_0 is unstable. Introducing a second equilibrium at $X = X_1$, we know that $\dot{X}(+\infty) \to +\infty$; indicating $\dot{X}(X' + \delta X) > 0$, hence X_1 is also unstable. Lastly, introducing a third equilibrium, from the preceding reasoning we know both the first and third equilibrium are unstable, leaving only one equilibrium to be potentially stable.

Lemma A.3 *The system X from Eq. 1.2 has multiple equilibria if and only if $a_1 < 0$, $a_2 > 0$ and $|a_3| < \sqrt{-4a_2^3/(27a_1)}$.*

Proof: We know that system X does not have multiple equilibria if $a_1 > 0$. Additionally, we know that setting $a_1 = 0$ reduces system X to a linear system, for which dX/dt by definition has only one root, and thus one equilibrium. From this we conclude that $a_1 < 0$ is a necessity for system X to have a regime with multiple equilibria.

Secondly, we need a regime where $d^2X/dt^2 > 0$, as otherwise the time evolution of X would be monotonously decreasing and thus have only one root. This yields

$$\frac{d^2X}{dt^2} = 3a_1X^2 + a_2 > 0 \Rightarrow |X| > \sqrt{-a_2/(3a_1)}; \tag{A.3}$$

given $a_1 < 0$ and $a_2 \neq 0$, this only yields real solutions if $a_2 > 0$. We conclude that $a_2 > 0$ is the second condition for system X to have a regime with multiple equilibria.

Lastly, we must find the values of a_3 for which there are multiple equilibria, i.e. real solutions for dX/dt. If the discriminant of the cubic equation is equal or greater than zero, the equation has only real-valued roots with at least one multiple, or three distinct real-valued roots respectively. The system has multiple equilibria if and only if all roots are real-valued and non-equal, so only the latter satisfies this condition. The cubic discriminant for polynomials of the form $ax^3 + bx^2 + cx + d = 0$ is given by

$$\Delta = 18abcd - 4b^3d + b^2c^2 - 4ac^3 - 27a^2d^2. \tag{A.4}$$

For the reduced cubic equation of system X we thus have

$$\Delta = 4a_1a_2^3 - 27a_1^2a_3^2 > 0. \tag{A.5}$$

Taking into account both other conditions, the system has multiple equilibria if and only if $|a_3| < \sqrt{-4a_2^3/(27a_1)}$.